NACA RM E53G17

NACA

RESEARCH MEMORANDUM

EXPERIMENTAL INVESTIGATION OF AN AXIAL-FLOW COMPRESSOR INLET STAGE OPERATING AT TRANSONIC RELATIVE INLET MACH NUMBERS

III - BLADE-ROW PERFORMANCE OF STAGE WITH TRANSONIC ROTOR AND SUBSONIC STATOR AT CORRECTED TIP SPEEDS OF 800 AND 1000 FEET PER SECOND

By Francis C. Schwenk, Seymour Lieblein, and George W. Lewis, Jr.

Lewis Flight Propulsion Laboratory
Cleveland, Ohio

NATIONAL ADVISORY COMMITTEE FOR AERONAUTICS

WASHINGTON

September 18, 1953
Declassified October 14, 1957

NATIONAL ADVISORY COMMITTEE FOR AERONAUTICS

RESEARCH MEMORANDUM

EXPERIMENTAL INVESTIGATION OF AN AXIAL-FLOW COMPRESSOR INLET STAGE OPERATING AT TRANSONIC RELATIVE INLET MACH NUMBERS III - BLADE-ROW PERFORMANCE OF STAGE WITH TRANSONIC ROTOR AND SUBSONIC STATOR AT CORRECTED TIP SPEEDS OF 800 AND 1000 FEET PER SECOND

By Francis C. Schwenk, Seymour Lieblein, and George W. Lewis, Jr.

SUMMARY

As a continuation of the investigation of a transonic, axial-flow compressor inlet stage designed for a rotor tip relative Mach number of 1.1, a series of survey tests was performed at corrected tip speeds of 800 and 1000 feet per second to permit a detailed analysis of the flow across the individual blade rows. The analysis is presented in a manner which provides design information for similar stages. The extensive blade-element data presented include the variations with incidence angle of such factors as losses, turning angle, axial velocity ratio, work coefficient, and efficiency.

At the minimum-loss incidence angle, apparently no measurable shock losses occurred in the rotor tip region as a result of operation at rotor-inlet relative Mach numbers up to about 1.04. However, the high inlet Mach numbers did reduce the range of the low-loss incidence angle in the rotor tip region. A pronounced compressibility effect existed at the higher levels of pressure ratio and Mach number and caused a reduction in the axial velocity ratio across the rotor as the blade speed was increased. Consequently, as the blade speed increased, the work coefficient and diffusion factor (blade loading) also increased. Measured blade-element characteristics of the subsonic stator blades were comparable with the characteristics of conventional airfoil sections in cascade. It was found that for this compressor configuration the assumption of simple radial equilibrium adequately described the radial variations of the rotor- and stator-outlet flow conditions. The mass-averaged rotor performance was presented and compared with the over-all stage performance.

INTRODUCTION

In view of the marked advantages associated with an extension of conventional Mach number limitations in axial-flow compressor design (ref. 1), an investigation was initiated to explore the feasibility of designing inlet-stage rotors to operate at higher-than-conventional relative inlet Mach numbers. A transonic inlet stage consisting of a transonic rotor and subsonic stators was designed and constructed for operation at a rotor tip relative inlet Mach number of 1.1. A description of the compressor and the results of the over-all performance of the stage as determined from fixed rake measurements at the compressor outlet are reported in reference 1. Further details of the geometry of the stage and specific blade-coordinate data are presented in reference 2.

In the second phase of the investigation, radial survey instruments were provided downstream of the rotor and stator to obtain the performance and flow characteristics of the individual blade rows and to provide design information for similar stages. The results of the survey measurements and mass-averaged performance over a range of compressor weight flows at corrected tip speeds of 800 and 1000 feet per second are reported herein. Results and analysis are presented in a form readily adaptable to current design procedure. Extensive blade-element loss and turning-angle characteristics as well as radial distributions of flow are presented. Information concerning radial pressure equilibrium, wall boundary-layer blockage, and mass-flow shifts as well as a comparison with design conditions are presented.

SYMBOLS

The following symbols are used in this report: A diagram illustrating the air and blade angles and the velocities is presented in figure 1 to more completely define some of the symbols used.

A_f compressor frontal area based on rotor tip diameter, 1.646 sq ft

a velocity of sound, ft/sec

c_p specific heat of air at constant pressure, Btu/(lb)($^\circ$R)

c_v specific heat of air at constant volume, Btu/(lb)($^\circ$R)

D diffusion factor

g acceleration due to gravity, 32.17 ft/sec^2

H total enthalpy, $c_p g J T$, sq ft/sec^2

i	incidence angle, angle between inlet-relative-air-velocity vector and a tangent to blade mean line at leading edge, deg
J	Joule's constant, 778.26 ft-lb/Btu
K	wall boundary-layer blockage factor
M	absolute Mach number
M'	relative Mach number
P	total pressure, lb/sq ft
P'	total pressure relative to a blade row, lb/sq ft
p	static pressure, lb/sq ft
r	radius measured from axis of rotation, in.
T	absolute total temperature, ^{o}R
U	blade speed, ft/sec
V	absolute velocity of air, ft/sec
V'	velocity of air relative to a blade row, ft/sec
W	weight flow of air, lb/sec
β	absolute air-flow angle measured from axis of rotation, deg
β'	air-flow angle relative to a blade row measured from axis of rotation, deg
γ	ratio of specific heats for air, c_p/c_v, 1.3947
γ^{o}	blade angle, direction of tangent to blade mean camber line at leading or trailing edge, deg
Δ	symbol used to indicate change in a quantity
δ	ratio of inlet total pressure to NACA standard total pressure, $P_1/2117$
δ^{o}	deviation angle, angle between outlet-relative-air-velocity vector and tangent to blade mean-line angle at trailing edge, deg
η	temperature-rise efficiency

θ ratio of compressor-inlet total temperature to NACA standard temperature, $T_1/518.6$

θ° air turning angle, change in the relative flow angle from inlet to outlet of a blade row, deg

ρ static density of air, lb/cu ft

σ solidity, ratio of blade chord to blade spacing

Φ camber angle, difference between directions of blade mean camber line at leading and trailing edges, deg

φ rotor-inlet flow coefficient, $V_{z,3}/U_3$

$\bar{\omega}$ relative total-pressure loss coefficient (appendix A)

ψ pressure coefficient (appendix B)

Subscripts:

av average

b blade element

f free stream

h hub

m mean radius

R rotor

ref reference

S stator

t tip

z axial direction

θ tangential direction

0 total or stagnation conditions

1 depression tank

2 weight-flow measuring station upstream of rotor

3 rotor inlet

4 rotor outlet (or stator inlet)

5 stator outlet

6 compressor outlet (discharge measuring station)

APPARATUS AND PROCEDURE

A complete description of the design and the geometry of the transonic, axial-flow compressor inlet stage and its test-rig installation is presented in references 1 and 2. Tables I and II show the rotor- and stator-blade angles and solidities. A sketch of the 17.36-inch-tip-diameter compressor installation is shown in figure 2. Hub radii at stations 2, 3, 4, 5, and 6 are, respectively, 4.312, 4.411, 5.186, 5.186, and 5.186 inches.

Instrumentation

Compressor inlet. - Compressor-inlet total pressures and total temperatures were determined from four static-pressure taps (negligible depression-tank velocity) and from six thermocouples uniformly spaced in the inlet depression tank (station 1). Air flow through the compressor was determined by means of a thin-plate, open-end orifice located in the inlet piping upstream of the depression tank. As an additional method of determining the weight flow of air into the compressor, a radial static-pressure rake (fig. 3(a) and ref. 1) was located in the annulus 2.1 inches upstream of the rotor at station 2 (fig. 2). Weight flow at this station was determined from the radial variation of static pressure given by the rake, the inlet stagnation conditions, and a wall boundary-layer blockage allowance which was determined from surveys taken during initial runs of the compressor.

Rotor inlet. - At the rotor inlet (station 3), four static-pressure taps were located on both the inner and outer walls. Because of the projected taper of the rotor blade, the outer-wall taps were 0.70 inch upstream of the rotor leading edge; whereas the inner-wall taps were 0.40 inch upstream of the rotor leading edge. The radial static-pressure gradient at the rotor inlet (used for computing rotor-inlet velocities) was faired between these inner- and outer-wall static-pressure readings with the use of a similar radial variation as that given by the static-pressure rake at station 2. The rotor-inlet stagnation conditions were considered to be the same as the depression-tank conditions.

Rotor outlet. - Rotor-outlet conditions were determined from radial surveys of static pressure, total pressure, and flow angle and from

fixed thermocouple rakes located about 1/2 inch downstream of the rotor (station 4). Since the variation of rotor-outlet air angle was expected to be relatively small for the two tip speeds investigated, two, fixed, 6-tip thermocouple rakes (fig. 3(b)) instead of surveys were used to determine rotor-outlet temperatures. The two temperature readings, taken at each of six radii located at the centers of equal-annular areas, were averaged and corrected for local Mach number effects.

Total-pressure and flow-angle surveys were made with one combination claw and total-pressure probe shown in figure 3(c). The radial variation of rotor-outlet static pressure was sensed by an L-head Prandtl tube having four static-pressure orifices manifolded together (fig. 3(d)). The geometry of and the typical calibration curves for Prandtl type static probes are given in reference 3. At each radial position, the Prandtl tube was set at an angle corresponding to the flow angle, which was measured by the claw and total-pressure survey probe. In addition, there were four static-pressure taps on both the inner and outer walls.

Stator outlet. - Stator-outlet survey data (angles and total and static pressures) were taken with similar instruments and with the same procedure as used for measuring rotor-outlet flow conditions. The claw and total-pressure and L-head static-pressure survey probes were located axially 1/2 inch downstream of the stator-blade trailing edge and circumferentially midway between adjacent stator blades. Temperatures for the stator outlet were obtained from two fixed thermocouple rakes (fig. 3(b)) located at station 6.

In order to obtain a more complete picture of the total-pressure field behind the stators, the following additional fixed instruments were installed:

(1) Three, radial, wall boundary-layer rakes (fig. 3(e)) were spaced relative to the stator blades, as illustrated in figure 4, for both the inner and outer walls. There were nine total-pressure tubes on each rake at 1/8-inch increments.

(2) Four circumferential wake rakes (fig. 3(f)) were placed behind the stator trailing edge at radii of 8.18, 7.28, 6.58, and 5.73 inches (fig. 5). The spacing between the tubes was approximately 0.05 inch.

(3) Two kiel probes (fig. 3(g)) were located at the mean radius (r_5 = 6.933 in.) and spaced to split the stator-blade passage in thirds (fig. 5).

All the instruments described were calibrated for the effects of flow angle and Mach number in a free jet, and when necessary all readings were corrected for these effects. Inasmuch as the rotor- and stator-outlet survey stations were located in constant-area portions of the

annulus, no corrections were made for the effects of radial flows on the survey measurements. Pressures were measured by manometers containing tetrabromoethane, and the thermocouple potentials were measured with a potentiometer balanced with a spotlight galvanometer.

Reliability. - In general, the evaluation of the specific accuracy or reliability of each particular measurement is an extremely difficult task. In addition to the usual errors involved in the sensing device, the recording apparatus, the calibration, and the reading process, which are to some extent amenable to quantitative evaluation, errors or discrepancies undoubtedly exist in compressor measurements because of interference and unsteady-flow effects. The orders of magnitude of these latter effects, in the present state of knowledge, are largely unknown. In order to minimize interference effects and measurement errors introduced by the finite size of instruments, all probes (see fig. 3) were designed with small frontal area. Some quantitative information about the effects of probe size on the accuracy of measurements can be found in reference 4.

The most reasonable evaluations of the reliability of the measurements are believed to be the comparisons between integrated weight flows computed from the survey data and weight flows determined by means of the inlet orifice, and the comparisons between temperature-rise and momentum efficiencies. For all test points, the integrated weight flows determined from data taken at station 2 (upstream of the rotor) agreed within 1 percent with the orifice weight flows, while the integrated weight flows for the rotor- and stator-outlet stations agreed within 2 percent with the weight flows as determined from the orifice measurements. As usual in single-stage compressor tests, the mass-averaged rotor momentum efficiencies were not greater than 2.5 percent higher than the mass-averaged rotor temperature-rise efficiencies. A comparatively higher momentum efficiency is to be expected, because the calculation of the actual work done based on the momentum concept does not include the work required to overcome the effects of the casing viscous drag forces (which appear in the measured temperature rise). Although random errors could conceivably be mutually cancelling and produce good weight-flow and efficiency checks, the continued appearance of satisfactory comparisons in an investigation may be accepted statistically as evidence of reliable measurements.

Procedure

For the survey tests of the transonic, axial-flow compressor stage, only two rotor corrected tip speeds were investigated: $U_t/\sqrt{\theta}$ = 1000 feet per second (design) and 800 feet per second. At each of these blade speeds, the stage was tested at five, different, corrected specific weight flows selected to cover the range of operation of the stage.

During the running of each test point, complete surveys of angles, total pressures, and static pressures were taken as described in the Instrumentation section of this report.

The inlet total pressure (depression tank) was held at 20 inches of mercury absolute, and the inlet total temperature varied between 79° and 85° F for the different test points. The blade tip speed was maintained constant within 1 percent of the desired values by an electronic speed control. At these inlet conditions and $U_t/\sqrt{\theta}$ = 1000 feet per second, the average rotor-blade-chord Reynolds number (for the weight-flow range covered) was 1.044×10^6 at the tip of the rotor and 0.748×10^6 at the hub. For the tests at $U_t/\sqrt{\theta}$ = 800 feet per second, the average Reynolds numbers were 0.871×10^6 at the tip and 0.620×10^6 at the hub.

Computations

The various equations and terms used in computing the blade-element and over-all performance of the stage are presented in the appendixes.

APPROACH

The basic design procedure for an axial-flow compressor stage involves two major phases: (1) the determination of the velocity diagrams which will produce the desired performance (pressure ratio, weight flow, and efficiency) and (2) the selection of the blading which will produce the desired outlet conditions (velocities, angles, and work input). In general, the complete compressor blade is constructed by a radial stacking of individual blade sections or elements.

The establishment of the design outlet conditions by a blade row will depend on the turning angles and losses (efficiency) of the blade sections or elements and the requirements of radial equilibrium and continuity for the annulus. Loss and turning-angle characteristics as functions of the blade incidence angle for given blade shapes are generally obtained from stationary- or rotating-cascade data. For conventional inlet stages, the concept of simple radial equilibrium $\left(\frac{dp}{dr} = \frac{\rho V_\theta^2}{gr}\right)$ has been found to be a satisfactory description of the equilibrium conditions for design purposes. Furthermore, for inlet stages, the flow in the annulus can be divided into two separate regions: the free-stream (low-loss) region covering the major portion of the blade height, and the relatively smaller boundary-layer (high-loss) region at the end walls. Since current design calculations consider only the free-stream conditions in determining the outlet-flow distributions, account must be taken of the reduced weight flow occurring in the

wall boundary-layer regions. For convenience, an area blockage factor is applied to the continuity equation to compute the annulus area required to pass the design mass flow and produce the desired free-stream flow conditions.

The approach used in the analysis given in this report was directed primarily toward supplying basic information required for the design of similar axial-flow compressor stages. Consequently, the description of the flow characteristics of both the rotor- and stator-blade rows for the operating range of this stage will be presented in the following manner: (1) the inlet conditions to the blade rows (to establish inlet angles and Mach numbers), (2) the blade-element characteristics as a function of the blade incidence angle (to establish turning angles and losses), (3) the radial distribution of flow properties leaving the blade rows including wall boundary-layer blockage factors and radial equilibrium, and (4) the mass-averaged performance (efficiency and total-pressure ratio).

ROTOR PERFORMANCE

Inlet Conditions

All computations of inlet conditions were made with the absolute inlet velocity considered axial in direction (no inlet guide vanes). Preliminary surveys at the rotor inlet revealed no evidence of any inlet rotation.

As mentioned in reference 1, account was taken in the rotor design for a radial variation of inlet velocity induced by curvature of the hub contour and the inlet bellmouth. In figure 6 is shown the measured radial variation of inlet absolute Mach number plotted as the ratio of Mach number to mean-radius Mach number. The design radial variation is also shown. Except for the hub region, the assumed variation agrees closely with the measured inlet Mach number gradients. It is also noted that a change in tip speed from 1000 to 800 feet per second appeared to have very little effect on the radial variation of inlet absolute Mach number, although a decrease in the gradient is observed at the lower weight flows for each tip speed.

The measured and design radial variations of inlet relative Mach number and inlet relative air angle are shown in figures 7 and 8, respectively. Blade angles at the rotor inlet are also shown in figure 8. At a tip speed of 1000 feet per second, the data at a corrected specific weight flow of 27.8 lb/(sec)(sq ft) were taken as representative of the peak-efficiency operation of the stage. When the data measured at peak efficiency are compared with the design flow conditions (design weight flow is 29.6 lb/(sec)(sq ft)), it is noted that (1) the mean-radius

absolute Mach number at the rotor inlet is 0.534 (design value is 0.60), (2) the relative inlet Mach numbers are about 0.05 lower than the design values (fig. 7), and (3) the relative inlet air angles are about 2.5° higher than the design values (fig. 8). Figure 8 shows also that the rotor operated with a radial variation of incidence angle which was somewhat greater than the design variation.

The effects of neglecting the radial variation of absolute inlet Mach number were investigated by calculating the relative air angles which would exist if the inlet absolute velocity were assumed constant over the radius. Again with $U_t/\sqrt{\theta}$ = 1000 feet per second and $W_1\sqrt{\theta}/\delta A_f$ = 27.8 lb/(sec)(sq ft) as the basis for comparison, it was found that, with a constant inlet absolute velocity, the relative air angles would be 2° higher than the measured values at the tip and 2° lower at the hub. Angle differences of this magnitude may be important in the proper setting of the rotor blades for high Mach number operation.

Blade-Element Characteristics

Blade elements as used in the presentation of the data and the description of the blade geometry are defined as those sections of a blade which lie on stream surfaces of revolution formed by rotating meridional streamlines about the compressor axis. For simplicity, it has been found satisfactory for this rotor to assume that the flow across each blade row occurs along conic surfaces with the ratio of stream tube height (radial distance between streamlines) to radial passage height ($r_t - r_h$) remaining constant at inlet and outlet. Thus, at all measuring stations, $\frac{r - r_h}{r_t - r_h}$ = constant, where r is the radius at which the streamline intersects the plane of measurement.

Selection of performance parameters. - In general design usage, blade sections at various radial positions are selected to produce the change in direction of the air flow (turning angle) required by the blade-row velocity diagram with a minimum of total-pressure loss at the particular design condition. The turning angle (or deviation angle) and loss characteristics of individual blade elements therefore constitute the basic design properties of a given blade section. Another significant factor in the blade-element performance is the ratio of outlet to inlet axial velocity. With the turning angle and the axial velocity ratio known, the rotor work input (change in absolute tangential velocity) is determined; and from the loss data, the element efficiency and the total-pressure ratio are then obtained. Although in low-speed two-dimensional cascades the axial velocity ratio is approximately 1, it may not generally be the case in the compressor configuration. Changes in axial velocity ratio over the compressor operating range may exert

significant effects on stage performance. Furthermore, in analyzing the blade-element losses, it is desirable to include the effects of blade loading and relative inlet Mach number.

Accordingly, the principal blade-element characteristics for the analysis were considered to be the variations with incidence angle of (1) air turning angle θ°, (2) outlet deviation angle δ°, (3) relative total-pressure loss coefficient $\bar{\omega}_R$ (eq. (A7), appendix A), (4) ratio of outlet to inlet axial velocity $V_{z,4}/V_{z,3}$ (measure of deviation of the velocity diagram from the two-dimensional incompressible-flow configuration), (5) work coefficient $\Delta H/U_t^2$ (a nondimensional temperature rise, eq. (B2), appendix B), (6) adiabatic temperature-rise efficiency η_b (eq. (A1), appendix A), (7) diffusion factor D_R (a blade-loading parameter described in ref. 5), and (8) relative inlet Mach number M_3'. The large number of parameters used was believed desirable in order to present a more complete evaluation and analysis of the element flow. Furthermore, the complete velocity diagrams for each element can be reconstructed from the information supplied.

Rotor-blade-element characteristics were determined at five streamline positions at radii spaced equally across the passage. A summary table of the geometry of each rotor-blade element is presented in table I. The end radial positions (4 and 8) were outside of the wall boundary layers. Blade-element characteristics were not determined in the wall boundary-layer regions because of the breakdown of the blade-element concept in these regions. The basic blade-element characteristics of these five rotor sections are shown in figure 9, and a detailed analysis of the variations of blade-element total-pressure loss, air turning angle, work coefficient, and efficiency will be presented subsequently.

Relative total-pressure loss coefficient. - In general, for a given compressor blade element, the loss in total pressure across the element is a function primarily of the blade loading (suction-surface velocity gradients) as it affects the surface boundary-layer growth, the relative inlet Mach number (compressibility effects), and the local three-dimensional flows (end effects and secondary flows). For the transonic compressor, the primary concern lies in the compressibility effects. Compressibility affects rotor losses in two principal ways: (1) by increasing the blade loading and (2) by causing shock waves with possible boundary-layer separation. (Losses associated with the external wave patterns and the shock entropy rise are generally quite small in the transonic range.) The effects of compressibility in increasing the suction-surface velocity gradients (blade loading) and consequently the surface boundary-layer growth for isolated airfoil sections are well known from the typical gradual increases in drag coefficient with inlet Mach number (up to the limiting value). In the compressor configuration, the compressibility effects on blade loading may be more pronounced

than for the isolated airfoil inasmuch as both the turning angle and the axial velocity ratio across the element may vary with inlet Mach number.

The second compressibility effect, that of shock losses, occurs when the local shock waves on the blade surfaces become sufficiently strong to cause a separation of the surface boundary layer behind the shock. The presence of shock-induced separation losses is generally indicated by a relatively sharp rise in the magnitude of the losses. The inlet Mach number at which the sharp rise in loss occurs is referred to as the limiting Mach number. In the analysis of rotor-blade-element losses, therefore, attention will be directed toward discussing both compressibility effects and obtaining design information such as best incidence angle, range, and limiting values of loading. The analysis is conducted in terms of a total-pressure loss coefficient taken relative to the rotating-blade element as developed in reference 5 and appendix A.

The computed variations of rotor relative total-pressure loss coefficient with incidence angle shown in figure 9 are typical of the loss characteristics of airfoil sections in general. Near the tip of the rotor (fig. 9(a)), two major changes in the loss characteristics occur as the compressor tip speed (and consequently relative inlet Mach number) is increased from 800 to 1000 feet per second, namely, a decrease in the low-loss range of incidence angle, particularly on the low-incidence side, and a marked rise in minimum loss coefficient. The sharp rise in loss coefficient at low incidence angles is also observed at a radius of 7.515 inches (fig. 9(b)). However, at least for the range covered, there appears to be little change in loss-incidence variations for the sections between the hub and mean radii as the speed is increased.

The effect of increasing the inlet Mach number on reducing the low-loss range of the element at low-incidence angles is not surprising, because results of tests of a similar blade section in a two-dimensional cascade revealed a similar effect. The loss characteristics of a double circular-arc blade section in cascade operated over a range of inlet Mach numbers up to 0.8 reported in reference 6 are shown in figure 10 for comparison. The sharp increase of the losses at low-incidence angles is believed due to the effects of a rapid acceleration of the flow about the leading edge on the pressure surface (with resulting shock formation and flow separation) and to possible choking of the blade passage. As in the case of the cascade section, the inlet Mach number had a considerably smaller effect on the range of the rotor loss curve for high-incidence angles (fig. 9(a)).

It is also noted that, according to the high Mach number loss characteristics of several other profile shapes reported in reference 6, the profiles whose points of maximum thickness occurred closer to the leading edge (British C4 thickness distribution on a circular-arc mean line)

show a considerably shorter range on the high-incidence-angle side as well as on the low side. The profile thickness distribution may therefore have a significant effect on rotor characteristics in the transonic range of operation.

In view of the relatively narrow range of operation of the high Mach number elements, it is necessary to determine the design (minimum-loss) incidence angle of the element within close limits. For the transonic rotor investigated, minimum loss occurred at an incidence angle of 2° in the tip region and at about 6° in the hub region. The incidence values used in the rotor design were 2° and 4° near tip and hub, respectively. Furthermore, it is also desirable to account for the effects of possible radial gradients of inlet velocity on the design relative inlet air angle. As mentioned in the Inlet Conditions section, an error of about 2° in the relative air inlet angle would have resulted in the tip region if the radial variation of the inlet absolute velocity had not been included in the design.

In determining the minimum-loss incidence angle over a range of inlet Mach numbers, it should be noted that a tendency exists for the minimum-loss point to shift several degrees to higher values of incidence angle as the rotor tip speed is increased from 800 to 1000 feet per second. Although a design-point shift in the transonic range is not conclusively demonstrated by the limited data presented for this rotor or by the cascade data of reference 6, unpublished data taken at the Lewis and Langley laboratories have shown this effect to exist.

Blade loading. - Although a strong temptation exists to attribute the increase of the general loss level in the tip region at 1000 feet per second (fig. 9(a)) to possible shock losses at the higher level of inlet Mach number, it must be recognized that the blade loading on the element is also increased at the higher tip speed. (The blade loading in the two-dimensional cascade configuration (fig. 10) remains approximately constant over the Mach number range.) Inasmuch as blade-element losses are generally influenced by both blade loading and shock losses, it is therefore desirable to attempt to evaluate the relative effects of the increases of the two quantities.

A recently developed parameter which effectively serves to correlate blade-element losses with blade loading at design incidence angle in the absence of shock losses is the diffusion factor D presented in reference 5. The diffusion factor serves as a rough measure of the element suction-surface velocity gradient and as such indicates the blade-element loading. In terms of the rotor velocity diagram, the diffusion factor is given by

$$D_R = \left[\left(1 - \frac{V_4'}{V_3'}\right) + \frac{V_{\theta,3}' - V_{\theta,4}'}{2\sigma_R V_3'}\right] \quad (1)$$

In reference 5, data from a large number of single-stage axial-flow compressors were shown to exhibit similar variations of blade-element loss with diffusion factor in the good (low-loss) range of incidence angle.

The variation of blade-element total-pressure loss coefficient with diffusion factor in the low-loss range of incidence at the five principal radial survey positions is shown in figure 11. In order to permit a comparison with the tip-region data of reference 5, which were obtained for points located about 10 to 12 percent of the passage height from the outer wall, an additional plot of loss coefficient against diffusion factor is presented in figure 11(a) for an outlet radius of 8.300 inches (about 11 percent from tip). The range of the loss-against-diffusion-factor data reported in reference 5 for rotors operating below their critical inlet Mach numbers is also shown by the dashed lines in figure 11(a) for blade elements in the tip region.

From figures 11(a) and (b) it is seen that the data from the tests fall within the limits of the data of reference 5, and the data for both tip speeds lie on a common curve of loss against diffusion factor. Therefore, in reference to the loss variation of figure 9(a) (r_4 = 8.098 in.), the increase in the minimum loss at 1000 feet per second over the minimum loss at 800 feet per second can be accounted for by the increased diffusion factor at the higher speed. It may be concluded, therefore, that at the Mach number level of the investigation (up to 1.04), the shock waves on the blade surfaces at the minimum-loss incidence angles do not yet appear to be sufficiently strong to cause a large increase in loss.

It is also interesting to note that although the rotor pressure ratio and relative inlet Mach number in the tip region (about 1.55 and 1.04, respectively) are considerably greater than corresponding values in conventional subsonic designs, the actual blade-loading levels (as described by the diffusion factor) and loss-coefficient levels in this region at design incidence angle are not substantially different from those in many subsonic designs (ref. 5).

Rotor-blade-element losses for the sections between the hub and mean radii (figs. 11(d) to (f)), have quite a different variation with diffusion factor than those for the tip section (fig. 11(a)). In fact, the rotor data for these sections show an agreement with the trend of the two-dimensional cascade losses. Comparison of the loss-coefficient variations with diffusion factor at the region between the mean and tip radii (figs. 11(a) to (d)) demonstrates the effect of radial location of the blade section on the losses. In addition to the profile loss (the

the losses. In addition to the profile loss (the major influence at the mean section), the element loss near the tip also includes three-dimensional effects such as tip-clearance leakage and casing friction.

Deviation and turning angle. - On figure 9, both the turning-angle and the deviation-angle characteristics of the five rotor-blade elements are shown plotted against incidence angle. Both angle parameters are presented because either quantity can be used for analysis. The figure shows that the turning-angle variation is essentially linear with the incidence angle, as expected from cascade test results. Although there is some doubt about the angle data for the lowest incidence points at $U_t/\sqrt{\theta}$ = 1000 and 800 feet per second, the measured deviation angles are essentially constant with incidence angle, as might be expected from two-dimensional cascade performance at these high levels of solidity. For the two rotor-blade speeds investigated, the turning (or deviation) angles do not appear to vary with the changes in inlet Mach number and axial velocity ratio attending the change in wheel speed. Inasmuch as the transonic rotor-blade elements do not correspond to any fixed or standard camber shape (e.g., circular arc, parabolic, etc.), it was not possible to compare the deviation-angle characteristics of the rotor with an available design rule.

Work coefficient. - In order to place the temperature-rise variation on a nondimensional basis, an actual work coefficient $\Delta H/U_t^2$ (defined by eq. (B2), appendix B) is sometimes used for the correlation of the performance data of a given stage operating over a range of blade speeds and as a tool for stage matching analysis. Reference 7 gives an example of the use of the work coefficient and presents a relation which expresses the dependence of the work coefficient on the velocity diagram. It is stated (ref. 7) that the condition of geometrically similar velocity diagrams at all blade speeds is sufficient to insure that the work coefficient will not vary with blade speed for a given value of flow coefficient (defined as the ratio of rotor-inlet axial velocity to wheel speed).

In figure 9(a) (tip element), the plot of actual work coefficient against incidence angle (incidence angle can be directly related to flow coefficient as in eq. (B8), appendix B) shows that, at a given value of flow coefficient in the low-loss range, the actual work coefficient does become greater in this case as the blade speed is increased from 800 to 1000 feet per second. It can also be noted that this difference persists at the other rotor-blade sections (figs. 9(b) to (e)) but becomes progressively smaller for the sections nearer the hub.

In looking for reasons for the differences in the work-coefficient level and the radial variation of the difference, recourse was made to equation (B7), appendix B. It can be seen for these rotor-blade elements (with r_4/r_3 = constant, β_3 = 0, and with no change in deviation angle

with blade speed, β_4' = constant) that the only variables affecting the work coefficient in equation (B7) are the flow coefficient φ and the axial velocity ratio $V_{z,4}/V_{z,3}$. At all blade sections (fig. 9), the axial velocity ratio decreased with an increase in the blade speed; and, at a given value of flow coefficient, a decrease in the axial velocity ratio will increase the level of the work coefficient (see eq. (B7), appendix B). However, since the rotor-outlet relative air angle β_4' becomes smaller for the blade elements closer to the hub, the effect of the change in axial velocity ratio on increasing the change in V_θ will be reduced (eq. (B7)). Thus, near the hub, there is no appreciable increase in the work-coefficient level with blade speed (fig. 9(e)). The decrease in the axial velocity ratio with an increase in blade speed is due to the compressibility effects on the density ratio, which become quite pronounced at the high inlet Mach number and pressure-ratio levels experienced with the transonic compressor. The effect of axial velocity ratio also caused the increased loadings (diffusion factors) at the higher blade speed, as shown in figure 9.

The foregoing discussion makes it apparent that the design axial velocity ratio must be closely obtained in the actual case if this type of compressor is to operate with the desired energy input and efficiency. Furthermore, should the actual axial velocity be different from the design value, the work coefficient and the diffusion factor will show a greater variation from the design conditions at the tip of the rotor than at the hub for compressor rotors of this geometry (decreasing rotor-outlet relative angle from tip to hub).

Efficiency. - The resultant rotor-blade-element efficiency is a function of the magnitudes of the relative total-pressure loss coefficient, the work input, and the relative inlet Mach number as indicated by equation (A8), appendix A. For the two sections nearest the tip (figs. 9(a) and (b)), the maximum efficiency at $U_t/\sqrt{\theta}$ = 1000 feet per second decreased only slightly from that at 800 feet per second, because the increased losses were partly counterbalanced by an increased work-input level. For the other sections, there was no substantial variation with speed of the losses, work level, or efficiency for the two blade speeds investigated.

At a given blade speed, the variation of blade-element efficiency with incidence angle and the value of incidence angle at which the peak efficiency occurs will depend on the trends of loss and work input with incidence angle. Generally, the peak-efficiency incidence angle is somewhat greater than the lowest-loss incidence angle; however, for these elements (fig. 9), the two angles are practically coincident since the variation of work input with incidence is not great in the low-loss ranges.

Outlet Conditions

Pressure ratio. - In figure 12 are several examples of the radial variation of the rotor total-pressure ratio for both tip speeds. With the exception of the pressure-ratio gradient at the highest weight flow for $U_t/\sqrt{\theta}$ = 1000 feet per second, all the radial pressure-ratio variations exhibit similar trends of a radially increasing pressure ratio. A rotor pressure ratio of as high as 1.58 was obtained in the tip region at the higher tip speed. At $U_t/\sqrt{\theta}$ = 1000 feet per second, there is a greater radial gradient of total-pressure ratio than at 800 feet per second because, as mentioned previously in the Blade-Element Characteristic section, the blade-element work coefficient increases more rapidly near the tip with increasing speed than near the hub (fig. 9). The customary sharp reduction in total-pressure ratio from the free-stream values is observed in the inner- and outer-wall boundary-layer regions.

Compared with the other weight flows, the variation of the total-pressure ratio in the tip region for the highest weight-flow point at $U_t/\sqrt{\theta}$ = 1000 feet per second in figure 12 is a reflection of the reduced efficiency obtained in the tip region.

Absolute flow angle. - In figure 13 are the radial variations of the absolute rotor-outlet air-flow angles (stator-inlet angle) for three weight flows at each tip speed. In general, all the curves show a slight reduction in angle in the main region of the flow as the radius is increased. The sharp increase in outlet angle at the blade ends is the result of the reduced axial velocity components and secondary flows in the wall boundary-layer regions. The general similarity of the outlet-angle variations is to be expected inasmuch as (except for the low weight-flow point at $U_t/\sqrt{\theta}$ = 800 ft/sec) the radial variations of the blade-element deviation angle and the axial velocity ratio are similar over the range of incidence angles (fig. 9). At the low weight-flow point at $U_t/\sqrt{\theta}$ = 800 feet per second, the rising outlet angle in the upper half of the annulus is a reflection of the reduced axial velocity ratio resulting from the stalled operation in the tip region at this weight flow (see loss and axial-velocity-ratio variations at the maximum incidence angle shown in fig. 9).

Mach numbers. - The radial variations of relative and absolute rotor-outlet Mach numbers for both tip speeds are presented in figure 14. With the exception of the highest weight-flow point at $U_t/\sqrt{\theta}$ = 1000 feet per second, the absolute Mach number is essentially constant across the passage except for the sharp fall off in the wall boundary-layers. Further evidence of a high-incidence-angle, tip stalling condition at $W\sqrt{\theta}/\delta A_f$ = 20.1 lb/(sec)(sq ft) and $U_t/\sqrt{\theta}$ = 800 feet per second is shown by comparison of the relative Mach number variation at this point with

the variations at the other weight flows at both tip speeds. The Mach number levels leaving the rotor should offer no Mach number problems with the use of a conventional stator section behind this rotor.

Efficiency. - The radial variations of the blade-element temperature-rise efficiency (eq. (A1), appendix A) are shown in figure 15 for both blade speeds. For each weight flow at $U_t/\sqrt{\theta}$ = 1000 feet per second (figs. 15(a) to (c)), the efficiency decreased from a maximum value located between the hub and mean radii to a lower value near the tip. The influence of the wall boundary layers is again evidenced by the rapid fall off of efficiency near both the inner and outer walls (fig. 15).

Figure 15 (and fig. 9) shows that the blade-element efficiency near the tip varies over a wide range of values with changes in weight flow (or incidence angle); whereas the blade-element efficiency for the other rotor-blade sections remains relatively constant over the weight-flow range covered. These effects can be traced to the higher levels of inlet Mach number and the blade-loading characteristics of the blade elements near the rotor tip as explained in the Blade-Element Characteristics section. Also at $W\sqrt{\theta}/\delta A_f$ = 20.1 lb/(sec)(sq ft) and $U_t/\sqrt{\theta}$ = 800 feet per second (figs. 15(d) to (e)), there was a rather low efficiency near the rotor tip, which is another indication of the stalling condition already discussed. Therefore, it can be concluded from the results given in figure 15 that the over-all efficiency characteristics of the rotor will be governed largely by the characteristics of the tip section. In reference 8, a similar conclusion is reached for several, typical, subsonic inlet stages.

Radial equilibrium. - In computing the velocity diagrams for the initial design of the transonic rotor, radial variations of velocity and air-flow angle at the rotor outlet were determined on the basis of simple radial equilibrium of pressure as given by the equation

$$\frac{dp}{dr} = \frac{\rho V_\theta^2}{gr} \tag{2}$$

The derivation of equation (2) requires the assumptions that (ref. 9) (1) the flow is axially symmetric, (2) the viscous shear forces are zero, (3) the radial velocities are zero, and (4) the accelerations due to streamline curvature are zero. In order to evaluate the validity of the simple equilibrium assumptions for transonic rotors of this type, a comparison was made between the survey-measured radial static-pressure variations and a calculated variation obtained from equation (2) in the form

$$p - p_{ref} = \int_{r_{ref}}^{r} \frac{\rho V_\theta^2}{gr}\, dr \tag{3}$$

The mechanics of the calculation consisted in first assuming a radial static-pressure variation which passes through the measured value of static pressure at the outer wall; second, computing the integrand of equation (3) at five radial positions corresponding to the five streamline positions from the assumed static pressures and the measured absolute air angles, total pressures, and total temperatures; and third, numerically integrating equation (3) to determine a new static-pressure variation. This new static-pressure variation was then used in the second trial, and the preceding process was repeated until the calculated static-pressure variation agreed with the trial variation. One or two iterations were usually sufficient to produce a solution. Continuity of weight flow can then be satisfied by means of adjustment of the value of the reference static pressure p_{ref}.

The comparison between survey-measured radial variation of static pressure and computed simple radial-equilibrium variations at the rotor outlet (station 4) are shown in figure 16 for both tip speeds. The results of the comparison of figure 16 show very good agreement between the actual and computed static-pressure variations in the high-efficiency range of operation. The good agreement is to be expected, however, in view of the low aspect ratio of the blading (about 1.2) and the large axial spacing between blade rows. A relatively poor comparison (probably due to instrument error) is obtained in the tip region at the stalled weight-flow point of $W\sqrt{\theta}/\delta A_f$ = 20.1 lb/(sec)(sq ft) at 800 feet per second. For the high weight-flow runs, the computed gradients evidence a slight departure from the measured values in the hub region. It is expected that the effects of the neglected terms, the streamline curvature and the radial velocity, may assume importance in the hub region because of the hub curvature and the high velocities existing at the high weight flows. In view of the results of figure 16, the use of the condition of simple radial equilibrium appears to be a satisfactory assumption in the design of transonic rotors of similar performance and geometry.

Weight-flow distribution. - A comparison of the radial distributions of weight flow in the annulus before and after the rotor is shown in figure 17. In view of the particular interest in possible weight-flow shifts in the transonic region of operation, curves were presented for only the high weight-flow points at $U_t/\sqrt{\theta}$ = 1000 feet per second. The ordinate $\frac{\rho V_z r}{\rho_{0,1} a_{0,1}} \frac{(r_t - r_h)}{(r_t - r_{h,2})}$ and the abscissa, percentage of radial blade height, were used in order to factor out the differences in passage height at the inlet and the outlet and to offer a better visual comparison of the weight-flow distributions at the two measuring stations. The continuity equation and the streamline definition given in the description of the rotor-blade elements were employed to derive the ordinate for figure 17.

Figure 17(a) represents the highest rotor-inlet relative Mach number test point taken during this survey investigation, and figure 17(b) shows the data measured at approximately peak-efficiency operation of the rotor. For figure 17(a), relative inlet Mach numbers of 1.0 and greater were obtained across about 28 percent of the passage from the outer wall. At both operating conditions, there are apparently no great radial shifts of weight flow according to information determined at measuring stations 2 and 4. Of course, there is a slight shifting of the air flow toward the middle of the annulus as a result of the wall boundary layers at the rotor-outlet measuring station.

Averaged Performance

Pressure ratio and efficiency. - The mass-averaged rotor performance data are shown in figure 18 plotted against the corrected weight flow per unit frontal area (specific weight flow) as computed from the orifice data. Given in the plot are the mass-averaged rotor pressure ratio (eq. (A3), appendix A) and the mass-averaged temperature-rise efficiency (eq. (A2), appendix A).

At a corrected tip speed of 800 feet per second, a peak averaged temperature-rise efficiency of 0.92 was attained at a corrected specific weight flow of 22.6 lb/(sec)(sq ft). At 1000 feet per second, the value of peak averaged efficiency is somewhat uncertain in view of the high efficiency point at $W\sqrt{\theta}/A_f\delta$ = 28.9 lb/(sec)(sq ft) in figure 18(b). A more probable efficiency variation is given by the curve faired through the data points in the figure. A peak rotor efficiency of about 0.91 or 0.915 at a specific weight flow of about 28.5 lb/(sec)(sq ft) and at a pressure ratio of about 1.47 is indicated at 1000 feet per second. Peak averaged rotor pressure ratio at design speed was 1.50 at a weight flow of 25.5 lb/(sec)(sq ft). The latter point is very close to the unstable flow (stall) point of the stage at this speed. A reduction in range of weight flow for good operation at the higher tip speed compared with the lower speed is also observed.

In examining the mass-averaged performance of the rotor, it is convenient to keep in mind that the averaged performance represents a mass-weighted summation of the performance of the individual elements of the blade row. As indicated in the radial plots of performance in figure 15, by far the largest variation of efficiency with weight flow occurred locally in the tip region of the rotor. The variations of the averaged performance are therefore a reflection primarily of the tip-region performance of the rotor.

Wall boundary-layer blockage factor. - The wall boundary-layer blockage factor K is defined as the ratio of the actual weight flow passing through the annulus to the ideal weight flow that would result if the

wall boundary layers were not present and the free-stream flow conditions were extrapolated to the walls. The blockage factors were computed by numerical integration to determine the actual and ideal weight flows.

Upstream of the rotor, preliminary surveys indicated that the blockage factor K_2 varied with the weight flow between values of 0.985 and 0.990 for the range of conditions investigated. Downstream of the rotor, the boundary-layer blockage factor K_4 varied with tip speed and weight flow as indicated in the following table:

$U_t/\sqrt{\theta}$, ft/sec	$W\sqrt{\theta}/\delta A_f$, lb/(sec)(sq ft)	K_4
1000	29.4	0.96
	27.8	.95
	25.5	.95
800	26.4	0.97
	23.3	.96
	20.1	.93

An average measured value of rotor-outlet blockage factor is about 0.96 for operation of the rotor at or near peak efficiency.

Comparison with Design

With the results determined at peak efficiency at $U_t/\sqrt{\theta}$ = 1000 feet per second as the basis for comparison, the following differences between the design and the actual performances can be noted:

	Design point data	Actual peak efficiency data
$\frac{W\sqrt{\theta}}{\delta A_f}$, lb/(sec)(sq ft)	29.6	28.5
$(P_4/P_1)_{av}$	1.35	1.47
Efficiency	0.85	0.91

In view of the importance of obtaining good design control for rotors of this type, it is desirable to investigate some of the factors causing the differences between the design and the actual peak-efficiency performance.

Weight flow. - Although the measured incidence angles at peak efficiency and the design rotor incidence angles were equal, the peak-efficiency weight flow was about 3.7 percent lower than the design value $\left(\frac{W\sqrt{\theta}}{\delta A_f} = 29.6 \text{ lb/(sec)(sq ft)}\right)$. However, as was reported in reference 2, it was found that the rotor-blade-inlet angles as constructed were about 2° higher than the requested design values. The blade-angle difference accounts for much of the difference between the peak-efficiency weight flow and the design weight flow.

Pressure ratio. - Following the design procedure employed for this stage, agreement between the actual and the design rotor pressure ratios will depend on whether or not the blade sections produce the design turning angles and how closely the design assumptions of rotor efficiency and outlet blockage factor agree with the actual values. Reference to figure 9 indicates that the actual and the design turning angles are about equal. However, the actual values of blockage factor and efficiency were 0.96 and 0.91, respectively; whereas, the design assumptions were 0.92 for blockage factor and 0.85 for efficiency. As a consequence, in order that the continuity of weight flow be maintained, the actual ratio of rotor-inlet to -outlet axial velocities at design speed was lower than the design point ratio (see axial-velocity-ratio plots on fig. 9), and the change in absolute tangential velocity V_θ was correspondingly greater than the design values. Therefore, the higher actual work input and the higher actual efficiency explain why the measured rotor total-pressure ratio was greater than the design. Accurate values or assumptions of blockage factor, efficiency, and turning angle appear to be necessary for good design control of the velocity diagrams at the higher levels of total-pressure ratio.

Efficiency. - For this exploratory type of design, it was necessary to assume the efficiency on the basis of limited loss information and results of compressor tests which were not directly applicable to the transonic operating range. As more blade-element loss information of the type given in figures 9 and 11 becomes available, it is felt that better comparisons between the design and actual efficiencies of inlet-stage compressors will result through the direct use of blade-element loss data in the design.

STATOR PERFORMANCE

The discussion and the analysis of the stator-row performance will follow directly along the lines of the ROTOR PERFORMANCE section. The stator-inlet conditions are taken as the rotor-outlet conditions at station 4 as reported in the ROTOR PERFORMANCE section.

Blade-Element Characteristics

The blade elements for the stator are defined in the same manner as for the rotor, and the streamline radii are assumed to remain constant across the stator-blade row because of the constant hub radius (5.186 in.). For a stationary blade row, the parameters important for the description of the blade characteristics are considered to be the variations with incidence angle of: (1) the air turning angle θ°, (2) the outlet deviation angle δ°, (3) the wake total-pressure loss coefficient $\bar{\omega}_S$ (eq. (A9), appendix A), (4) the ratio of outlet to inlet axial velocity $V_{z,5}/V_{z,4}$, (5) the diffusion factor D_S, and (6) the inlet Mach number M_4. Blade-element characteristics were determined for four streamline positions at radii corresponding to the wake-rake locations as discussed in the Instrumentation section. A summary table of the stator-blade-element geometry for the streamlines under discussion is given in table II. The basic blade-element characteristics of the four stator sections are presented in figure 19.

Total-pressure loss coefficient. - The over-all loss in total pressure experienced by the air flow in passing through a stationary blade row situated downstream of a rotor consists of two separate effects: (1) a decrease in free-stream total pressure resulting from a turbulent mixing of air leaving the rotor (free-stream loss), and (2) the loss in total pressure caused by the build-up of a boundary layer on the stator-blade surfaces (wake loss). In view of the experimental difficulties involved in the accurate determination of the free-stream loss and because of the desirability of comparing the stator losses with cascade data, it was decided to conduct the stator loss study on the basis of the wake total-pressure loss coefficient $\bar{\omega}_S$ (eq. (A9), appendix A). The wake loss is computed from the difference between the free-stream and the average total pressures measured at the stator outlet. The average stator-outlet total pressure $P_{5,av}$ was computed by area averaging the circumferential variation of total pressure P_5. An example of one of these circumferential variations as measured by the stator-outlet instruments is shown in figure 20.

The variation of the wake loss coefficient with incidence angle for the four stator-blade elements (fig. 19) follows a trend similar to the loss variation for a typical airfoil section in cascade at comparable levels of inlet Mach number. The cascade data for an airfoil section quite similar in appearance to the stator sections appears in figure 10, and the general similarity between the loss characteristics of the stator and cascade configurations can be seen. There apparently is a change in the stator-loss-coefficient variation with incidence angle which depends on the radial location of the individual blade elements. For example, near the outer casing (fig. 19(a)) the loss-coefficient variation with

incidence presents a relatively shallow curve (wide incidence range), while comparatively, the loss variation near the hub (fig. 19(d)) is steep. An explanation for this feature might be found in the belief that the three-dimensional flows in a stator row tend to concentrate low-energy air at the annulus hub.

By comparison of the data measured for the two tip speeds, it can be noted that there apparently is no effect of inlet Mach number level on the form and magnitude of the stator-element wake loss coefficients for the range of data given. Because the change in Mach number level with speed is small (fig. 19) and because the measured Mach numbers are below the limiting Mach number for these sections, little influence from Mach number effects should be expected (note fig. 10 for comparison with cascade results).

The test results (fig. 19) indicate a value of about zero for the stator minimum-loss incidence angle, and this incidence angle occurred approximately at peak-efficiency operation of the rotor at design speed.

Blade loading. - Further comparison of the stator-blade-element losses with cascade losses depends on information concerning the blade-element loading or diffusion factor D_S. For the stator case, the diffusion factor can be written with the use of the velocity-diagram notation given in figure 1 as

$$D_S = \left[\left(1 - \frac{V_5}{V_4}\right) + \left(\frac{V_{\theta,4} - V_{\theta,5}}{2\sigma_S V_4}\right)\right] \tag{4}$$

The computed stator diffusion factors are given in figure 19. The slight increase in diffusion factor at the higher speed is a reflection of the reduced axial velocity ratio across the blade row (outlet angle remains constant). As in the case of the rotor, the reduced axial velocity ratio at the higher-speed level is a result of the increased compressibility effect.

For both blade speeds, the values of diffusion factor are less than 0.60, which was given as an approximate loading limit for two-dimensional, low-speed cascades in reference 5. Comparison of the minimum stator wake loss coefficients with cascade airfoil data (fig. 10 and ref. 5) shows that these measured minimum losses agree with the cascade results.

Turning and deviation angles. - Turning- and deviation-angle variations with incidence angle are presented in figure 19. However, these data must be accepted with some reservations, since the stator-outlet flow angles were determined for only one circumferential position located approximately midway between two blades. It is to be expected that this method will give a flow angle approximately equal to the true circumferentially averaged value only if the blade wakes are small.

With the exception of the hub section (fig. 19(d)) the turning-angle variation with incidence angle is linear, as might be expected from cascade test results. For the two levels of rotor speed investigated, the stator turning and deviation angles do not appear to vary with changes in inlet Mach number and axial velocity ratio as caused by the change in wheel speed.

Inasmuch as the stators are circular-arc elements, a comparison between the measured deviation angles and the deviation angles computed with Carter's rule for two-dimensional cascades of airfoils having a circular-arc mean camber line is given in figure 19. Carter's rule (ref. 10) is given by

$$\delta^{\circ} = m\Phi\sqrt{1/\sigma} \tag{5}$$

where m is a constant which depends on the blade-setting (chord) angle. Figures 19(b) and (c) show that the deviation angle remains constant with incidence angle and that an excellent agreement exists between the measured and calculated deviation angles in the midspan portion of the blade. Near the blade ends (figs. 19(a) and (d)), the deviation angle varies with incidence angle and the agreement with Carter's rule is not good, probably because of the proximity of the annulus walls to these elements and the accompanying three-dimensional effects. However, it may also be that the single survey measured values are not representative of the average angles in these regions.

Outlet Conditions

Several examples of the air-flow angle and the Mach number variations with radius for both tip speeds are given in figures 21 and 22, respectively. The angle information was determined by a single survey probe, and the Mach numbers were computed from faired static-pressure and faired circumferentially averaged total-pressure data. Except for the wall boundary-layer regions, the angles remain essentially constant over the annulus height and apparently vary only slightly with wheel speed and weight flow. One effect of the radially increasing total energy at the stator outlet is represented by the radial gradient of Mach number for the lower weight-flow points at each tip speed (fig. 22). The variation of Mach number with radius at $U_t/\sqrt{\theta}$ = 800 feet per second is smaller than at the higher tip speed because of the smaller energy gradient experienced at the lower tip speed.

Radial equilibrium. - A comparison between the computed radial equilibrium static-pressure variation and the measured static pressures is given in figure 23 for the stator outlet (station 5). Equation (3) was

employed for the computation by using a procedure similar to that described in ROTOR PERFORMANCE. In this case, the total pressures were taken from faired radial variations of circumferentially averaged stator-outlet total pressure. The agreement between the computed and the measured static-pressure variations is good and to some extent better than the radial equilibrium check at the rotor outlet (station 4). It is possible that the effects of radial velocities and streamline curvature, which were neglected in equation (3), are small in this particular case because the hub radius is constant for approximately 3 inches ahead of the stator outlet.

Weight-flow distribution and blockage factor. - The stator-outlet data were too limited to permit the accurate calculation of the weight-flow distributions and the wall boundary-layer blockage factors. However, in the free-stream region there was no indication of a radial shift of weight flow across the stator. The stator-outlet blockage factor K_5 was estimated to be about 0.95 or slightly smaller than the value for the rotor outlet.

OVER-ALL STAGE PERFORMANCE

The average over-all stage performance was computed on the basis of an area average of the stator-outlet total-pressure and total-temperature data. In order to make these results comparable with the over-all performance data of reference 1, the area-averaged performance was calculated by averaging the data determined at the centers of six equal-annular areas. The temperature readings were averaged directly; however, the total pressures were obtained from faired radial variations.

The area-averaged over-all stage total-pressure ratio and efficiency (eq. (A10), appendix A) are shown in figure 24 plotted against the corrected specific weight flow $W\sqrt{\theta}/\delta A_f$ as computed from the orifice measurements. The mass-averaged rotor performance is shown in figure 24 to facilitate the comparison between the rotor and the stage performance. Also given in this figure is the over-all performance for this stage, which was reported in reference 1. On the whole, the over-all performance computed from the survey test data compares well with that reported in reference 1. Some differences do appear in the efficiency variation, but these might be attributed to experimental inaccuracies and the different methods employed for determining the area-averaged total pressures and total temperatures at the stage outlet. The weight flows measured during the survey tests appear to be about 1 to 2 percent higher than the results given in reference 1. The weight-flow difference may be due to the use of a smaller-diameter orifice for the survey tests.

Although a comparison of the rotor and stage performance is not exactly correct because of the different averaging methods employed

(the data were insufficient to permit the computation of a mass-averaged performance at the stator outlet), at least an approximate idea of the effects of the stator losses can be determined from figure 24. Near peak efficiency, the stators caused a 2-percent decrease in efficiency at $U_t/\sqrt{\theta}$ = 1000 feet per second; whereas, at 800 feet per second, the decrease is generally somewhat greater. Since the stator loss-coefficient level was not materially affected by the tip speed level, it would be expected that the efficiency decrease due to the stator would be slightly greater at $U_t/\sqrt{\theta}$ = 800 feet per second because of the lower work level. Apparently, the rotor-blade characteristics and not the stator blades were the controlling feature with respect to the weight-flow range of this transonic compressor-inlet stage.

In order to generalize the stage performance, the over-all stage work input data were converted to a dimensionless form $\Delta H/U_t^2$ and this quantity and the stage efficiency are shown plotted in figure 25 against the mean-radius rotor-inlet flow coefficient $(V_{z3}/U_3)_m$. It can be noted that on an average basis, as well as for the rotor-blade elements (fig. 9), the work coefficient $\Delta H/U_t^2$ is higher at $U_t/\sqrt{\theta}$ = 1000 feet per second than at $U_t/\sqrt{\theta}$ = 800 feet per second. The variations of stage efficiency with the mean-radius flow coefficient again indicate the reduction in the incidence-angle range which occurred at the higher Mach numbers.

SUMMARY OF RESULTS

The following results were obtained from the survey tests of an experimental, transonic, axial-flow compressor inlet stage operating at corrected tip speeds of 1000 and 800 feet per second:

Analysis of the rotor-blade-row performance indicated that

1. A radial variation of absolute velocity existed at the rotor inlet. An error of 2° in the incidence angle would have existed at the rotor tip if the gradient of inlet velocity had been neglected for the design.

2. For the rotor tip section, a reduction in the low-loss range of incidence angle, particularly on the low-incidence side, was noted for the higher tip speed (inlet relative Mach numbers about 1.04). The reduced range is consistent with high-speed, two-dimensional cascade data.

3. In the tip region of the rotor, the magnitude of the minimum loss was greater for the higher (design) tip speed. However, on the basis of the analysis presented, the increased minimum losses were attributed

primarily to a greater blade loading at design tip speed. Apparently at this level of inlet relative Mach number (1.04), shock losses were not yet evident.

4. For the hub and mean sections, little change in the loss-incidence characteristics with tip speed (Mach number) was observed for the weight-flow ranges investigated.

5. The minimum-loss incidence angle for the blade section near the tip was 2° for the Mach number levels (1.04) experienced at a corrected rotor tip speed $U_t/\sqrt{\theta}$ of 1000 feet per second; whereas, at $U_t/\sqrt{\theta}$ = 800 feet per second, the minimum-loss incidence angle was somewhat lower than 2°. For the hub section, the minimum-loss incidence angle was about 6° at both wheel speeds.

6. The turning-angle - incidence-angle variations for all sections were essentially linear, with little apparent effect on the turning angles arising from changes in axial velocity ratio or Mach number.

7. Because of the pronounced compressibility effects existing at the higher levels of pressure ratio and Mach number, the axial velocity ratio across the rotor decreased with an increase in the blade speed, causing greater magnitudes of work coefficient and diffusion factor to occur at design speed. These effects were most pronounced in the tip region of the rotor.

8. Rotor-outlet (or stator-inlet) Mach numbers were essentially constant over the radius at a value of 0.65 for peak efficiency operation at $U_t/\sqrt{\theta}$ = 1000 feet per second.

9. At $U_t/\sqrt{\theta}$ = 1000 feet per second, the peak mass-averaged rotor temperature-rise efficiency of about 0.91 was attained at a corrected specific weight flow $W\sqrt{\theta}/\delta A_f$ of 28.5 lb/(sec)(sq ft) with a mass-averaged rotor total-pressure ratio of about 1.47. At $U_t/\sqrt{\theta}$ = 800 feet per second, the peak rotor efficiency was 0.92 at $W\sqrt{\theta}/\delta A_f$ = 22.6 lb/(sec)(sq ft) with a rotor total-pressure ratio of 1.28.

Analysis of the stator-blade-row performance indicated that

1. The stator losses were low and comparable to conventional stator and two-dimensional cascade losses. The minimum-loss incidence angle was about zero for all stator sections.

2. With the exception of the hub section, the stator turning angles varied linearly with incidence angle. The measured stator deviation angles for two sections located near the mean radius agreed closely with low-speed, two-dimensional cascade deviation angles as computed from

Carter's rule. There was no measurable effect of changes in axial velocity ratio and Mach number level on the measured turning (or deviation) angles.

Analysis of the performance of both blade rows indicated that

1. Radial static-pressure variations computed by assuming simple radial equilibrium agreed with the measured distributions for both the rotor-outlet and the stator-outlet stations.

2. At the Mach number levels experienced during the survey tests, there occurred no significant shifts in the weight-flow distribution across the rotor- and stator-blade rows.

3. The weight-flow range of the stage was controlled by the rotor-blade-row characteristics.

4. The important factors necessary for obtaining design control for similar stages were found to be: blade-element loss and turning-angle data, minimum-loss incidence angles, and wall boundary-layer blockage factors at the inlet and outlet of each blade row.

Lewis Flight Propulsion Laboratory
National Advisory Committee for Aeronautics
Cleveland, Ohio, July 20, 1953

APPENDIX A

ROTOR EFFICIENCY AND LOSS TERMS

Blade-element temperature-rise efficiency. - The adiabatic temperature-rise efficiency across a rotor-blade element is defined as the ratio of isentropic work input to actual work input based on total-temperature rise or

$$\eta_b = \frac{T_1\left[\left(\frac{P_4}{P_1}\right)^{\frac{\gamma-1}{\gamma}} - 1.0\right]}{T_4 - T_1} \tag{A1}$$

inasmuch as $P_3 = P_1$ and $T_3 = T_1$.

Mass-averaged temperature-rise efficiency. - The average temperature-rise efficiency for the rotor was computed as the ratio of the mass-weighted isentropic power input to the actual mass-weighted power input computed from the temperature rise across the rotor. The equation is

$$\eta = \frac{T_1\int_{r_{h,4}}^{r_{t,4}} \rho_4 V_{z,4} r_4 \left[\left(\frac{P_4}{P_1}\right)^{\frac{\gamma-1}{\gamma}} - 1.0\right] dr_4}{\int_{r_{h,4}}^{r_{t,4}} \rho_4 V_{z,4} r_4 (T_4 - T_1)\, dr_4} \tag{A2}$$

Mass-averaged total-pressure ratio. - The mass-averaged rotor total-pressure ratio was computed from the mass-weighted average isentropic power input by using the following equation:

$$\frac{P_4}{P_1} = \left\{ \frac{\int_{r_{h,4}}^{r_{t,4}} \left[\left(\frac{P_4}{P_1}\right)^{\frac{\gamma-1}{\gamma}} - 1.0\right] \rho_4 V_{z,4} r_4\, dr_4}{\int_{r_{h,4}}^{r_{t,4}} \rho_4 V_{z,4} r_4\, dr_4} + 1.0 \right\}^{\frac{\gamma}{\gamma-1}} \tag{A3}$$

Rotor relative total-pressure loss coefficient. - For the purposes of analysis of basic loss characteristics and the comparison of compressor rotor losses with the results of cascade tests, the blade-element relative total-pressure loss is more significant than the efficiency, which is a function of the work input level and the loss combined. The rotor relative total-pressure loss coefficient is defined as (ref. 5)

$$\bar{\omega}_R = \frac{P'_{4,ideal} - P_4'}{P_3' - p_3} \tag{A4}$$

Then, dividing by P_3', factoring, and substituting the Mach number function for p_3/P_3' yield

$$\bar{\omega}_R = \left(\frac{P_4'}{P_3'}\right)_{ideal}\left[\frac{1.0 - \frac{(P_4'/P_3')}{(P_4'/P_3')_{ideal}}}{1.0 - \left(1.0 + \frac{\gamma-1}{2} M_3'^2\right)^{-\frac{\gamma}{\gamma-1}}}\right] \tag{A5}$$

As shown in reference 6, the ratio P_4'/P_3' can be written in terms of the absolute total-temperature and -pressure ratios as follows:

$$\left(\frac{P_4'}{P_3'}\right) = \left(\frac{P_4'}{P_3'}\right)_{ideal}\left(\frac{P_4}{P_3}\right)\left(\frac{T_4}{T_3}\right)^{-\frac{\gamma}{\gamma-1}} \tag{A6}$$

Then the definition for rotor relative total-pressure loss coefficient becomes

$$\bar{\omega}_R = \left(\frac{P_4'}{P_3'}\right)_{ideal}\left[\frac{1.0 - \left(\frac{P_4}{P_3}\right)\left(\frac{T_4}{T_3}\right)^{-\frac{\gamma}{\gamma-1}}}{1.0 - \left(1.0 + \frac{\gamma-1}{2} M_3'^2\right)^{-\frac{\gamma}{\gamma-1}}}\right] \tag{A7}$$

The ideal relative total-pressure ratio $(P_4'/P_3')_{ideal}$ is a function of the element wheel speed and the change in radius across the blade

element. For these survey tests, the largest value of $(P_4'/P_3')_{ideal}$ encountered is 1.063 for the hub section at $U_t/\sqrt{\theta}$ = 1000 feet per second. Therefore $(P_4'/P_3')_{ideal}$ was assumed constant at 1.0 for the calculations of rotor relative total-pressure loss, because the resulting error is small compared with the usual experimental errors. Then, by combining equations (A1) and (A7), and with $(P_4'/P_3')_{ideal} \approx 1.00$, the rotor-blade-element efficiency can be expressed as

$$\eta_b = \frac{\frac{T_4}{T_3}\left\{1.0 - \bar{\omega}_R\left[1.0 - \left(1.0 + \frac{\gamma-1}{2} M_3'^2\right)^{-\frac{\gamma}{\gamma-1}}\right]\right\}^{\frac{\gamma-1}{\gamma}} - 1.0}{\frac{T_4}{T_3} - 1.0} \tag{A8}$$

Stator wake total-pressure loss coefficient. - For the analysis of the measured stator losses, the wake loss coefficient was employed. This quantity is defined as

$$\bar{\omega}_S = \frac{P_{5,f} - P_{5,av}}{P_4 - p_4} \tag{A9}$$

Area-averaged stage efficiency. - The stage adiabatic efficiency was computed from an area-weighted average of the stator-outlet total pressures and temperatures and can be expressed as

$$\eta = \frac{T_1\left[\left(\frac{P_5}{P_1}\right)^{\frac{\gamma-1}{\gamma}} - 1.0\right]}{T_6 - T_1} \tag{A10}$$

where

$$T_6 = T_5$$

APPENDIX B

WORK COEFFICIENT

The work coefficient is computed from the total temperature rise across the rotor-blade elements and is defined as

$$\frac{\Delta H}{U_t^2} = \frac{g J c_p T_{standard} \left(\frac{T_4 - T_1}{T_1} \right)}{\left(\frac{U_t}{\sqrt{\theta}} \right)^2} \tag{B1}$$

or in terms of the physical constants used for these tests

$$\frac{\Delta H}{U_t^2} = \frac{3.1455 \left(\frac{T_4 - T_1}{T_1} \right) 10^6}{\left(\frac{U_t}{\sqrt{\theta}} \right)^2} \tag{B2}$$

The work coefficient can be related to the total-pressure ratio as follows:

$$\frac{\Delta H}{U_t^2} = \frac{3.1455 \frac{1}{\eta} \left[\left(\frac{P_4}{P_1} \right)^{\frac{\gamma - 1}{\gamma}} - 1.0 \right] 10^6}{\left(\frac{U_t}{\sqrt{\theta}} \right)^2} \tag{B3}$$

or

$$\frac{\Delta H}{U_t^2} = \frac{1}{\eta} \psi \tag{B4}$$

The pressure coefficient ψ is defined as follows:

$$\psi = \frac{gJc_pT_{standard}\left[\left(\frac{P_4}{P_3}\right)^{\frac{\gamma-1}{\gamma}} - 1.0\right]}{\left(\frac{U_t}{\sqrt{\theta}}\right)^2} \tag{B5}$$

As described in reference 7, the element work coefficient can be written as a function of velocity-diagram parameters. With the use of the notation as given on figure 1, this expression becomes

$$\frac{\Delta H}{U_t^2} = \left(\frac{r_3}{r_t}\right)^2\left[\left(\frac{r_4}{r_3}\right)^2 - \left(\frac{r_4}{r_3}\right)\frac{V_{z,3}}{U_3}\frac{V_{z,4}}{V_{z,3}}\tan\beta_4' - \frac{V_{z,3}}{U_3}\tan\beta_3\right] \tag{B6}$$

or in terms of the flow coefficient $\varphi = V_{z,3}/U_3$

$$\frac{\Delta H}{U_t^2} = \left(\frac{r_3}{r_t}\right)^2\left[\left(\frac{r_4}{r_3}\right)^2 - \left(\frac{r_4}{r_3}\right)\varphi\frac{V_{z,4}}{V_{z,3}}\tan\beta_4' - \varphi\tan\beta_3\right] \tag{B7}$$

The flow coefficient φ can be related to the incidence angle by

$$i_R = \beta_3' - \gamma_{3,R}^{\circ} = \arctan\left(\frac{1}{\varphi} - \tan\beta_3\right) - \gamma_{3,R}^{\circ} \tag{B8}$$

REFERENCES

1. Lieblein, Seymour, Lewis, George W., Jr., and Sandercock, Donald M.: Experimental Investigation of an Axial-Flow Compressor Inlet Stage Operating at Transonic Relative Inlet Mach Numbers. I - Over-All Performance of Stage with Transonic Rotor and Subsonic Stators up to Rotor Relative Inlet Mach Number of 1.1. NACA RM E52A24, 1952.

2. Lewis, George W., Jr.: Experimental Investigation of Axial-Flow Compressor Inlet Stage Operating at Transonic Relative Inlet Mach Numbers. II - Blade-Coordinate Data. NACA RM E52C27, 1952.

3. Gettelman, Clarence C., and Krause, Lloyd N.: Characteristics of a Wedge with Various Holder Configurations for Static-Pressure Measurements in Subsonic Gas Streams. NACA RM E51G09, 1951.

4. Krause, Lloyd N., and Gettelman, Clarence C.: Effect of Interaction Among Probes, Supports, Duct Walls and Jet Boundaries on Pressure Measurements in Ducts and Jets. Paper No. 52-12-2, presented at Instrument Soc. Am. meeting, Cleveland (Ohio), Sept. 8-12, 1952. (To be published in Proc. Instrument Soc. Am.)

5. Lieblein, Seymour, Schwenk, Francis C., and Broderick, Robert L.: Diffusion Factor for Estimating Losses and Limiting Blade Loadings in Axial-Flow-Compressor Blade Elements. NACA RM E53D01, 1953.

6. Andrews, S. J.: Tests Related to the Effect of Profile Shape and Camber Line on Compressor Cascade Performance. Rep. No. R. 60, British N.G.T.E., Oct. 1949.

7. Medeiros, Arthur A., Benser, William A., and Hatch, James E.: Analysis of Off-Design Performance of a 16-Stage Axial-Flow Compressor with Various Blade Modifications. NACA RM E52L03, 1953.

8. Jackson, Robert J.: Effects on the Weight-Flow Range and Efficiency of a Typical Axial-Flow Compressor Inlet Stage that Result from the Use of a Decreased Blade Camber or Decreased Guide-Vane Turning. NACA RM E52G02, 1952.

9. Wu, Chung-Hua, and Wolfenstein, Lincoln: Application of Radial-Equilibrium Condition to Axial-Flow Compressor and Turbine Design. NACA Rep. 955, 1950. (Supersedes NACA TN 1795.)

10. Carter, A.D.S.: The Low Speed Performance of Related Aerofoils in Cascade. Rep. No. R. 55, British N.G.T.E., Sept. 1949.

TABLE I. - ROTOR-BLADE-ELEMENT GEOMETRY

Radial position	Radius, in.		Solidity, σ	Blade inlet angle, γ_3°, deg	Blade outlet angle, γ_4°, deg
	Inlet, r_3	Outlet, r_4			
4	7.969	8.098	1.32	53.5	31.0
5	7.257	7.515	1.44	51.1	27.0
6	6.546	6.933	1.57	48.5	21.7
7	5.834	6.350	1.72	45.6	15.5
8	5.123	5.768	1.91	42.6	7.8

TABLE II. - STATOR-BLADE-ELEMENT GEOMETRY

Wake-rake position	Radius, inlet r_4 and outlet r_5, in.	Solidity, σ	Blade inlet angle, γ_4°, deg	Blade outlet angle, γ_5°, deg
1	8.18	1.11	38.7	18.7
2	7.28	1.18	40.0	20.0
3	6.58	1.26	41.1	21.0
4	5.73	1.38	42.8	22.2

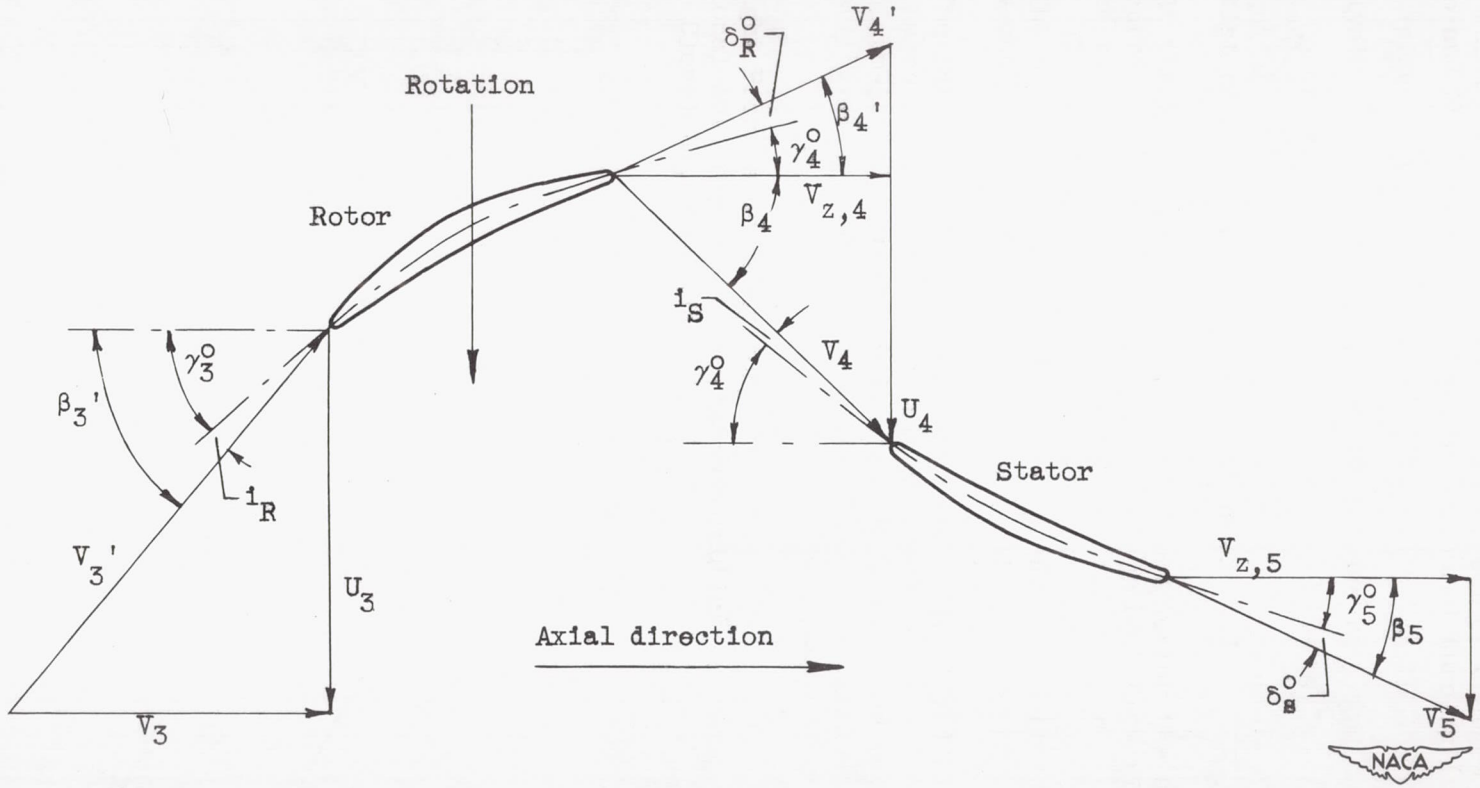

Figure 1. - Velocity-diagram notation for blade element.

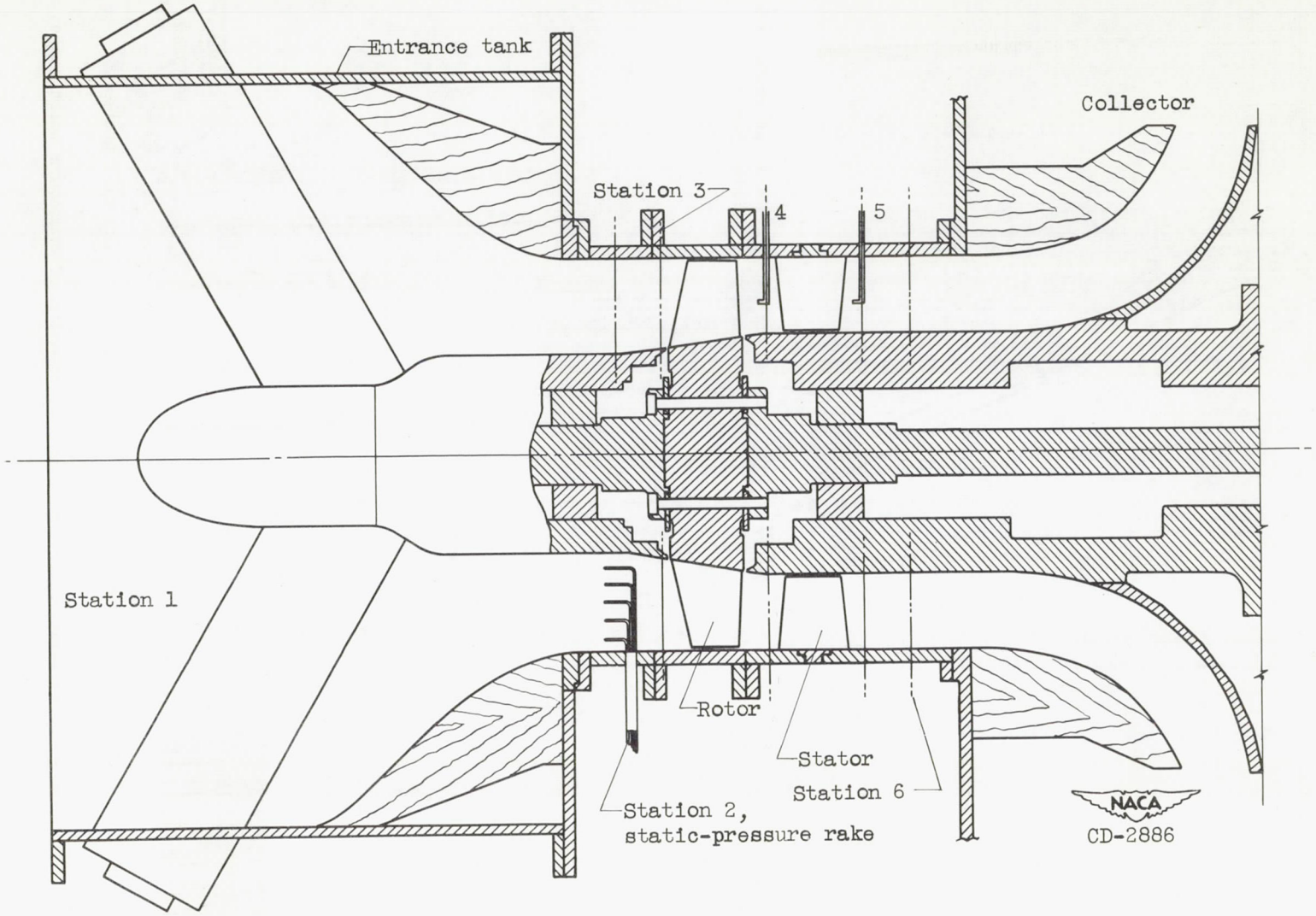

Figure 2. - Schematic diagram of variable-component transonic compressor test rig.

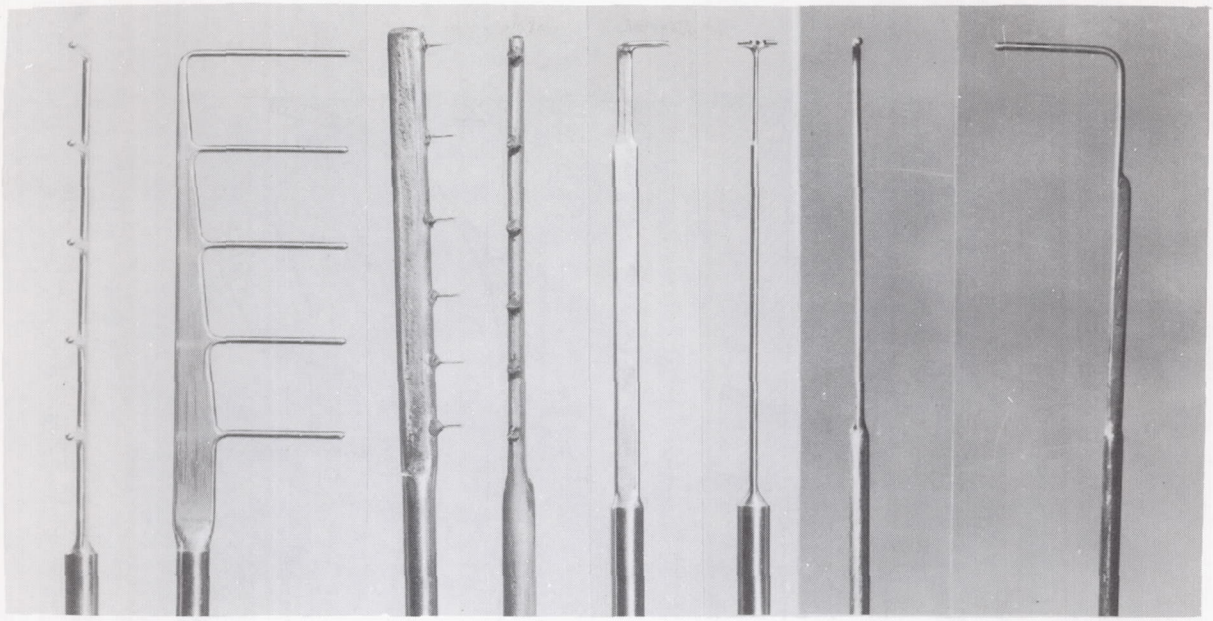

(a) Inlet static-pressure rake (b) Thermocouple rake (c) Claw and total-pressure survey probe (d) Static-pressure survey probe

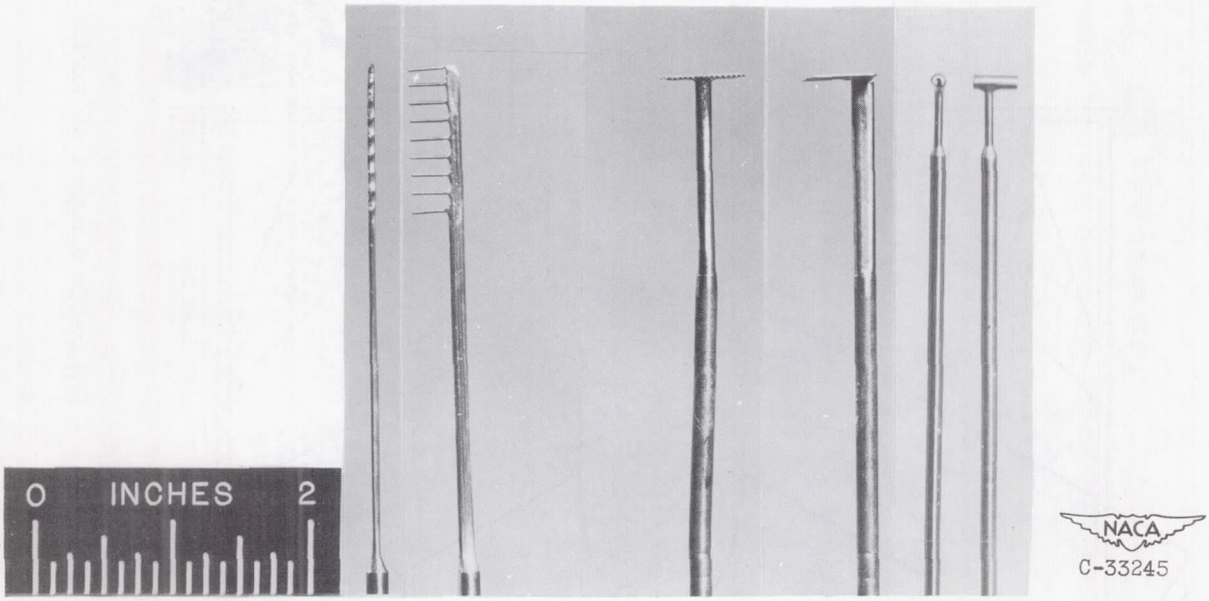

(e) Wall boundary-layer rake (f) Wake rake (g) Kiel probe

Figure 3. - Instrumentation used for investigation of transonic inlet stage.

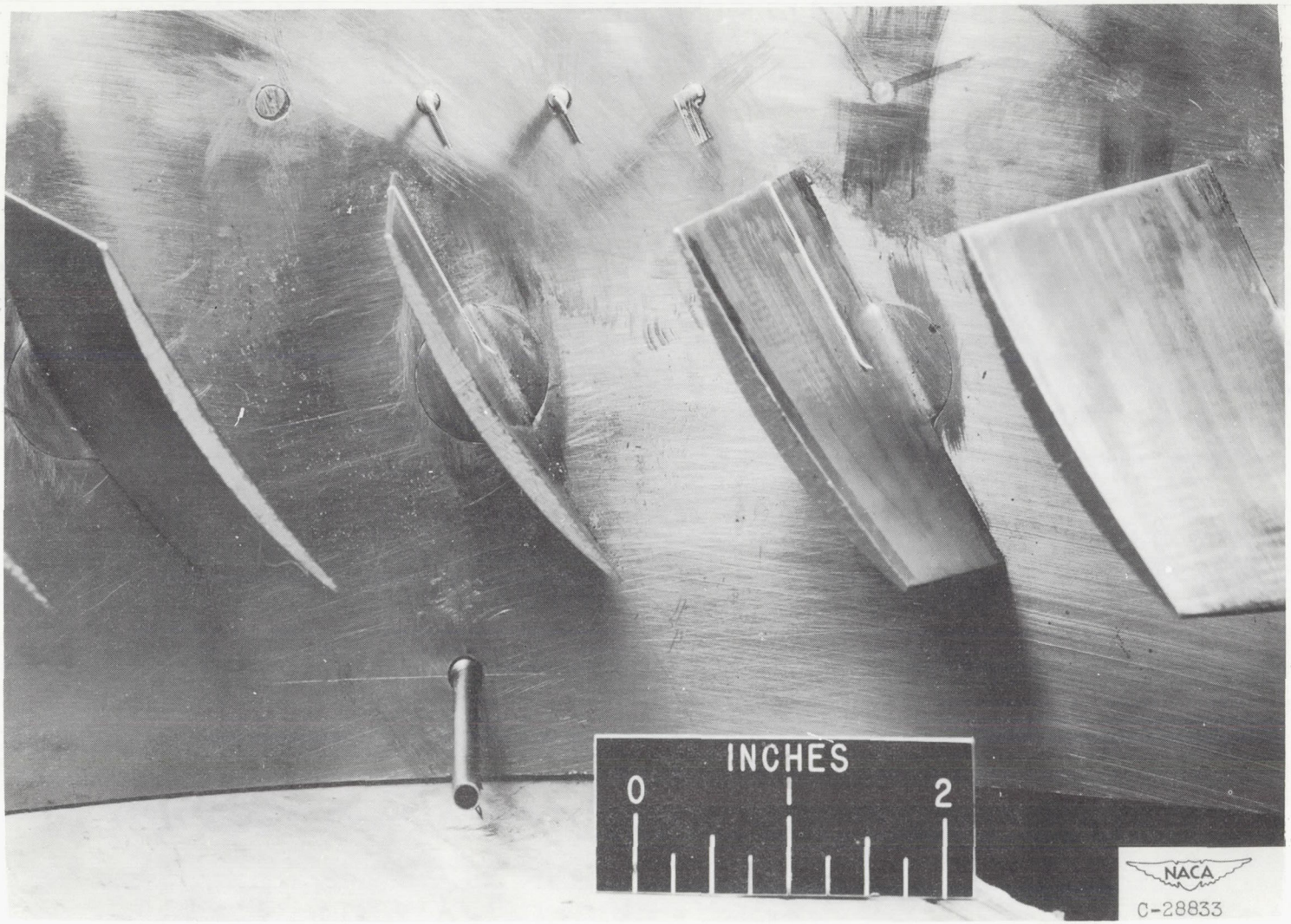

Figure 4. - Location of fixed wall boundary-layer rakes downstream of stators.

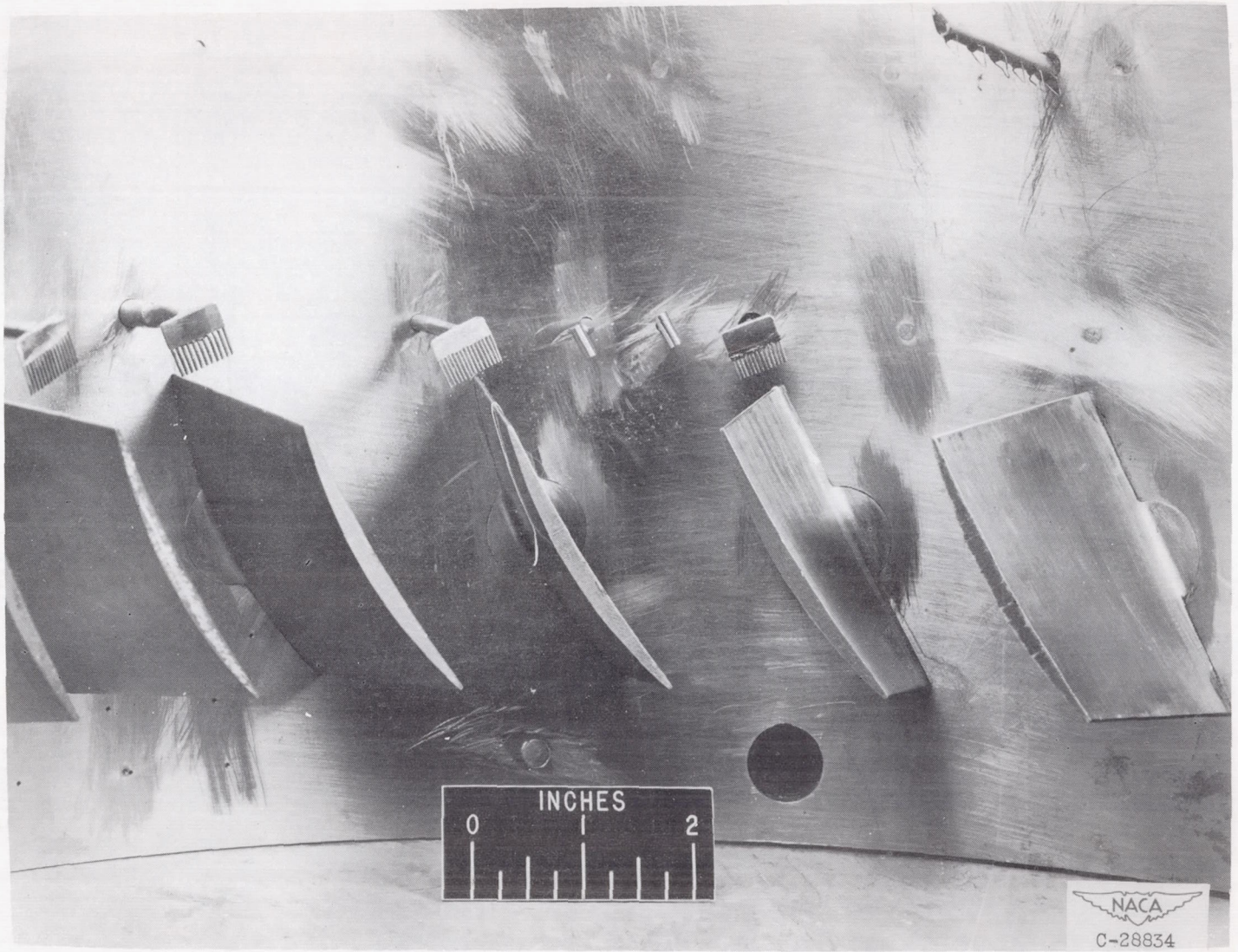

Figure 5. - Location of wake rakes and Kiel probes downstream of stators.

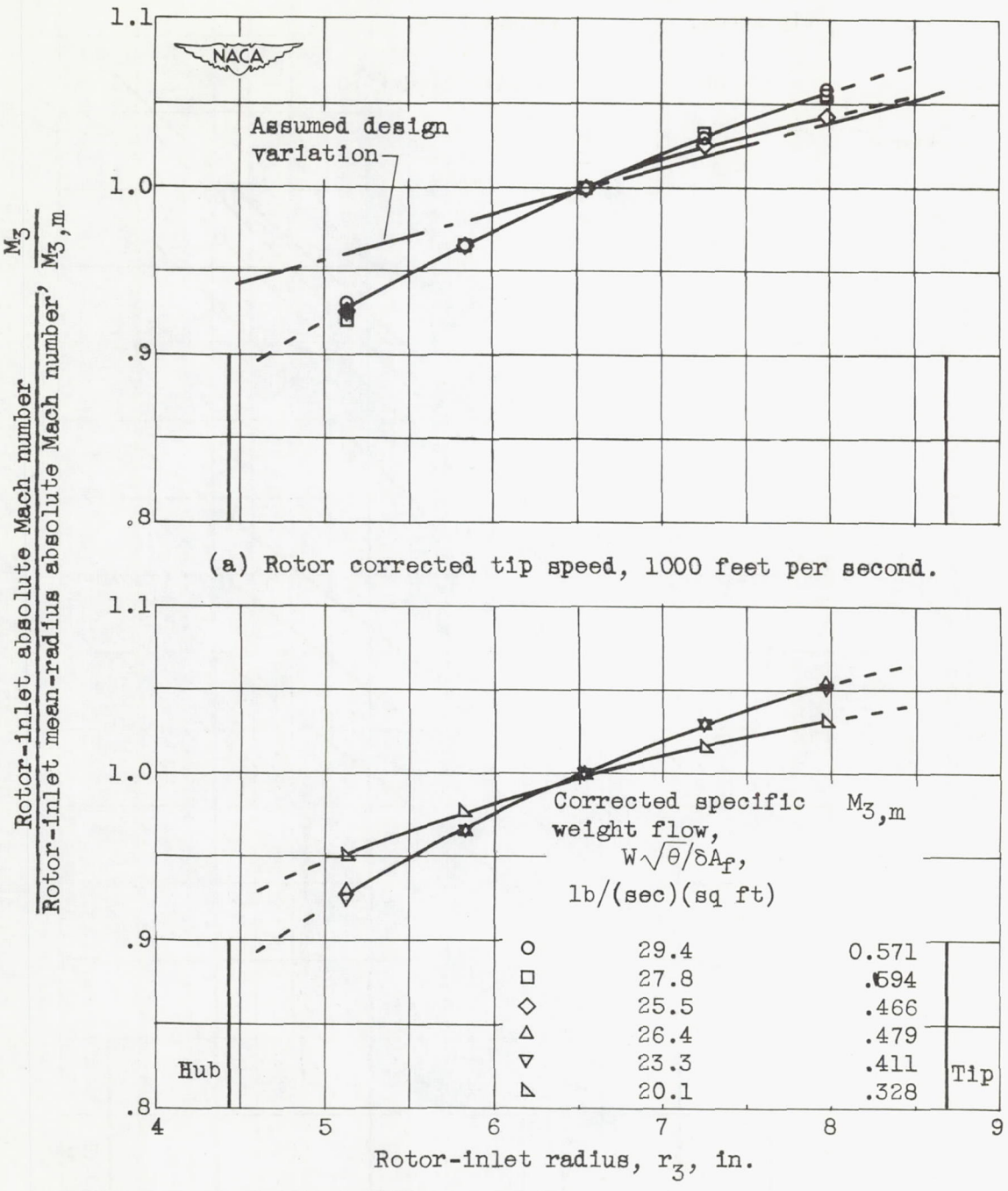

(a) Rotor corrected tip speed, 1000 feet per second.

(b) Rotor corrected tip speed, 800 feet per second.

Figure 6. - Radial variation of rotor-inlet absolute Mach number (station 3).

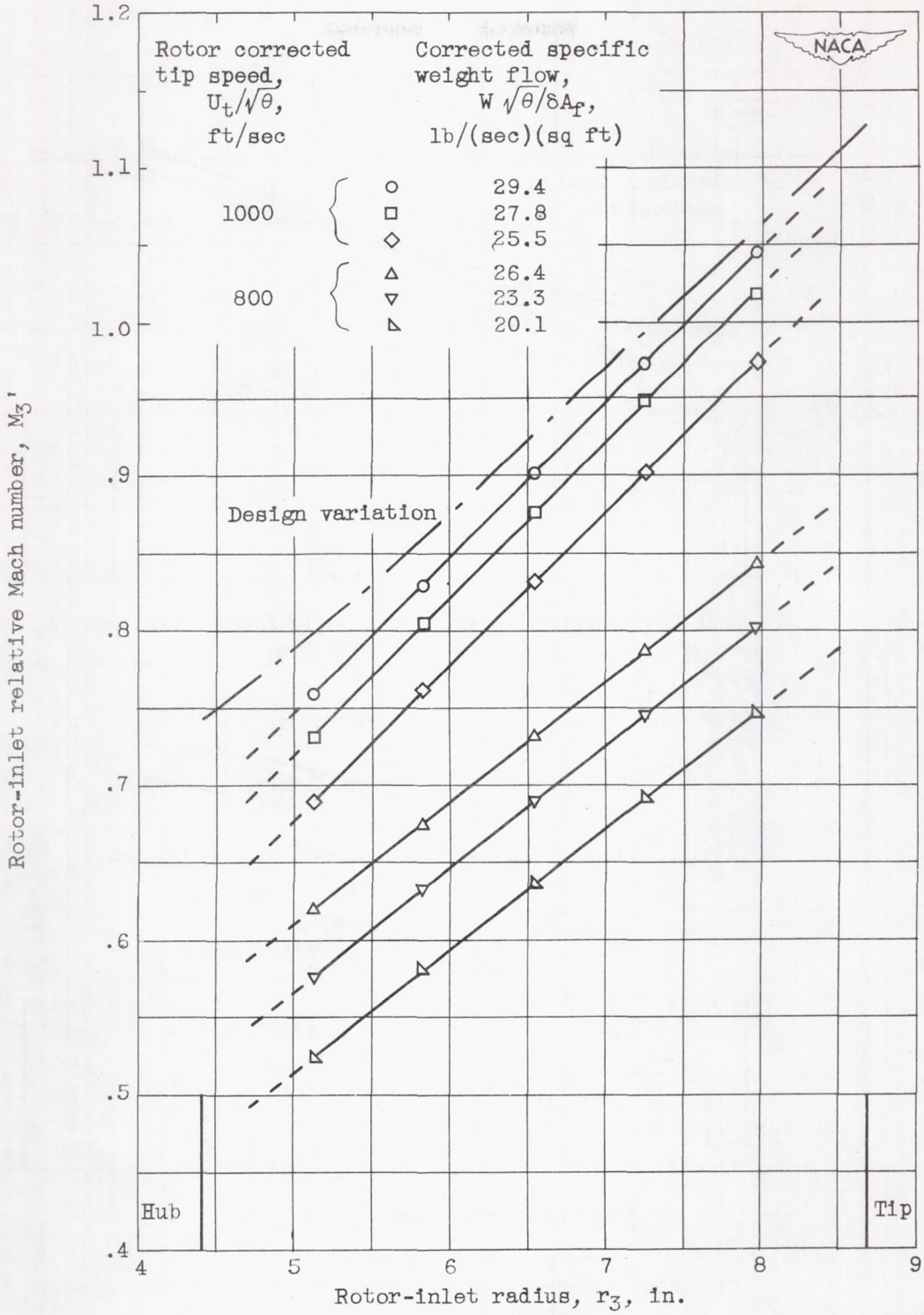

Figure 7. - Radial variation of rotor-inlet relative Mach number (station 3).

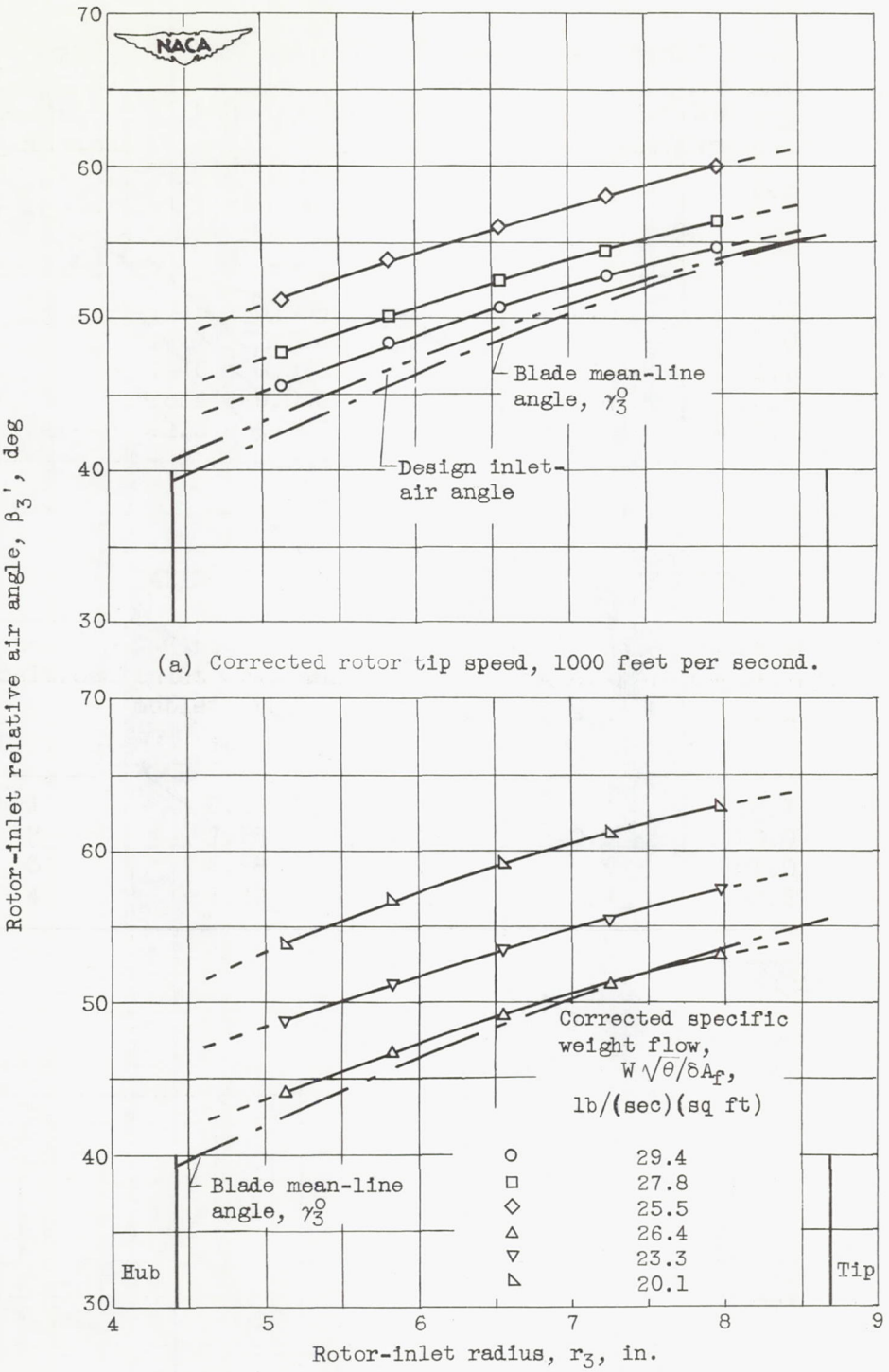

(a) Corrected rotor tip speed, 1000 feet per second.

(b) Corrected rotor tip speed, 800 feet per second.

Figure 8. - Radial variation of rotor-inlet relative air angles (station 3).

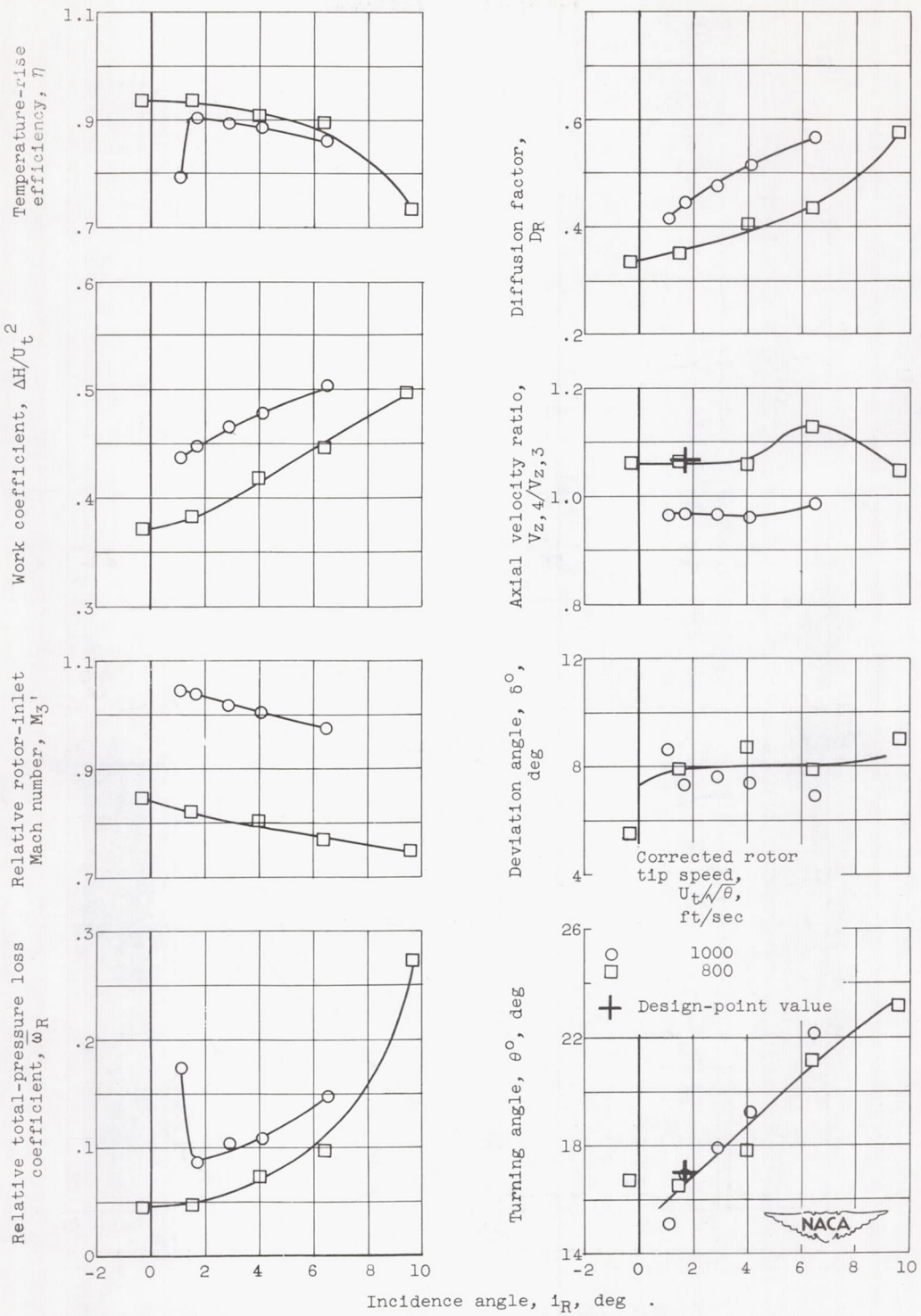

(a) Position 4; radius, 8.098 inches (near tip).

Figure 9. - Rotor-blade-element characteristics.

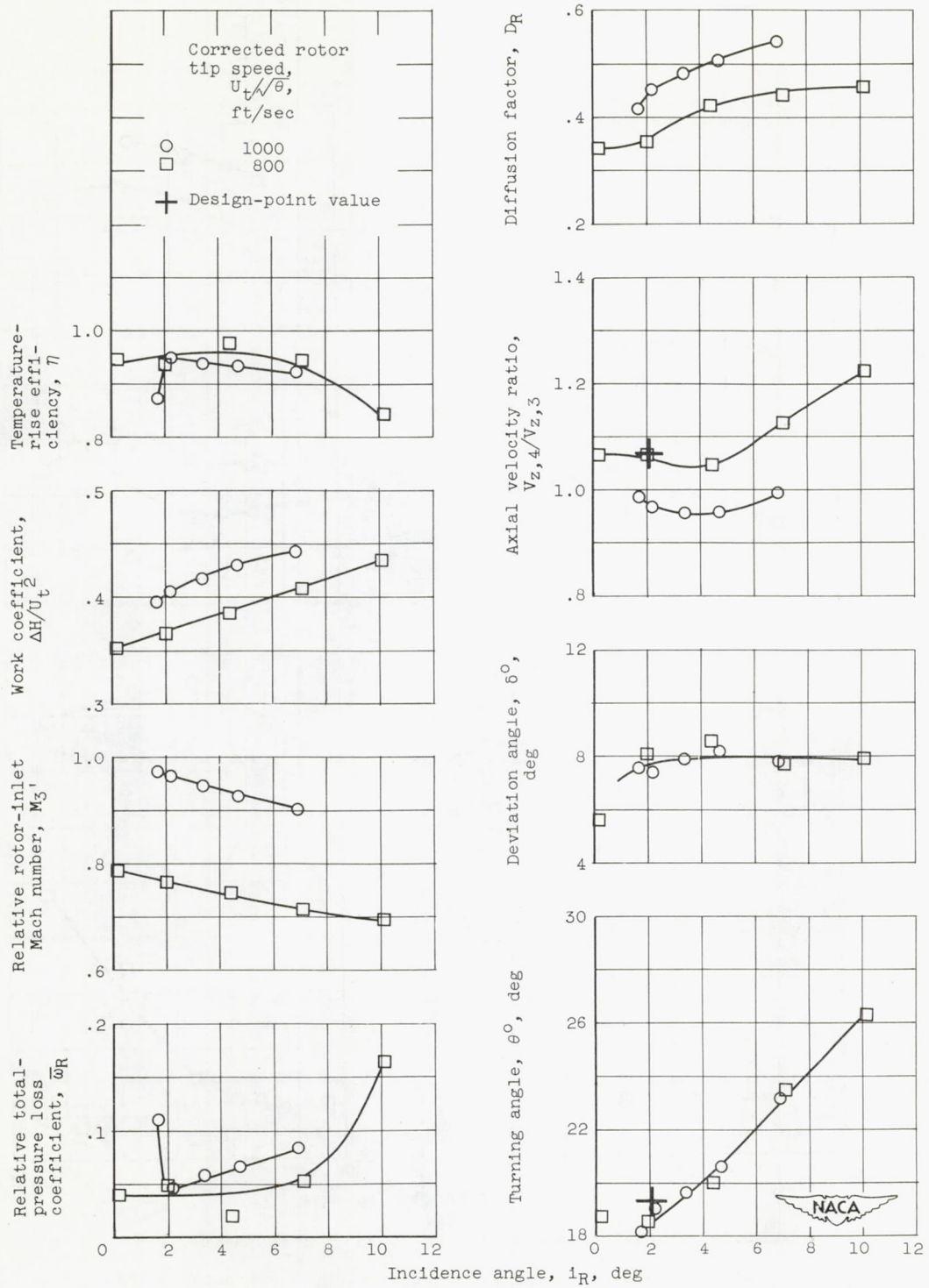

(b) Position 5; radius, 7.515 inches.

Figure 9. - Continued. Rotor-blade-element characteristics.

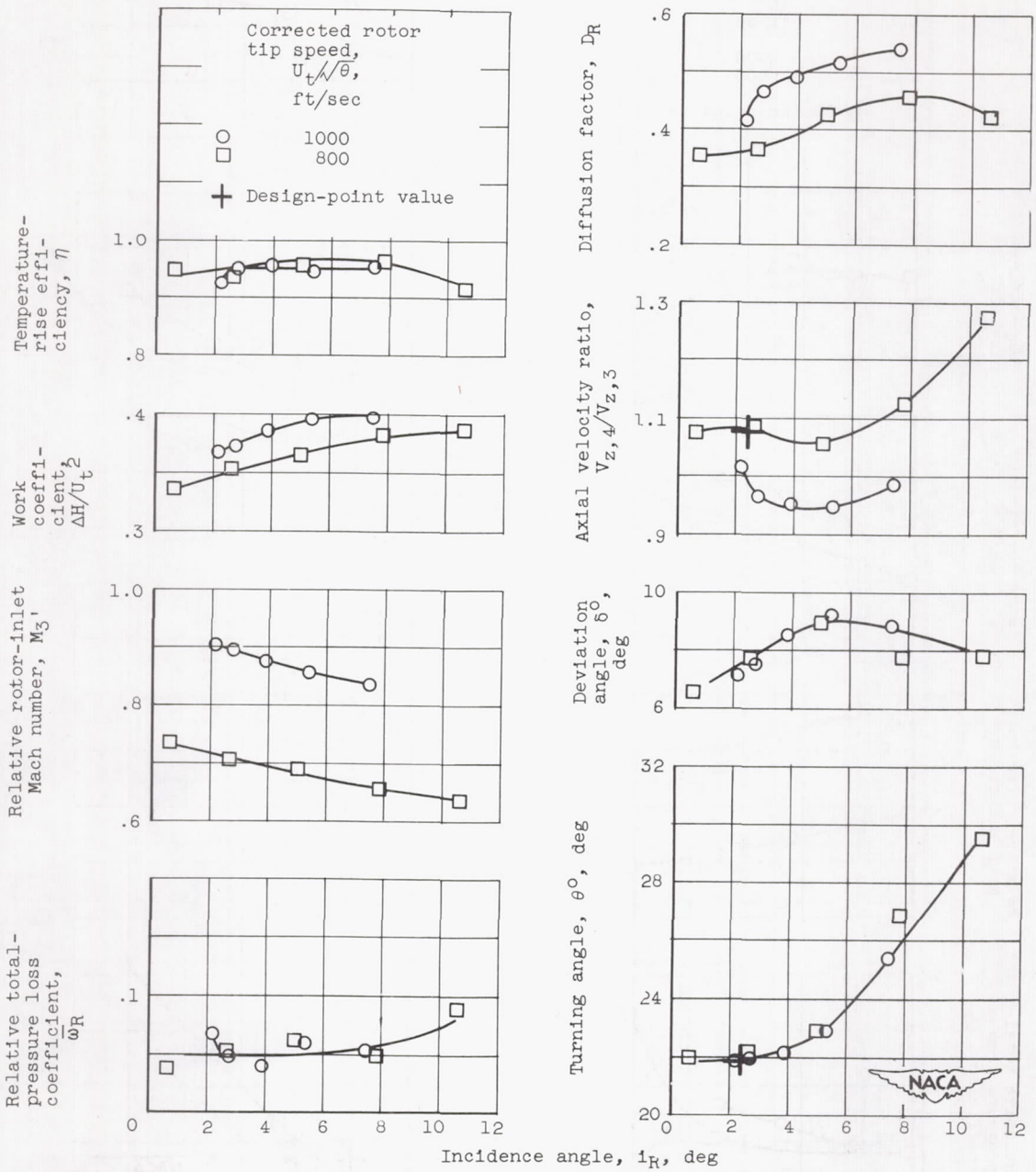

(c) Position 6; radius, 6.933 inches (mean).

Figure 9. - Continued. Rotor-blade-element characteristics.

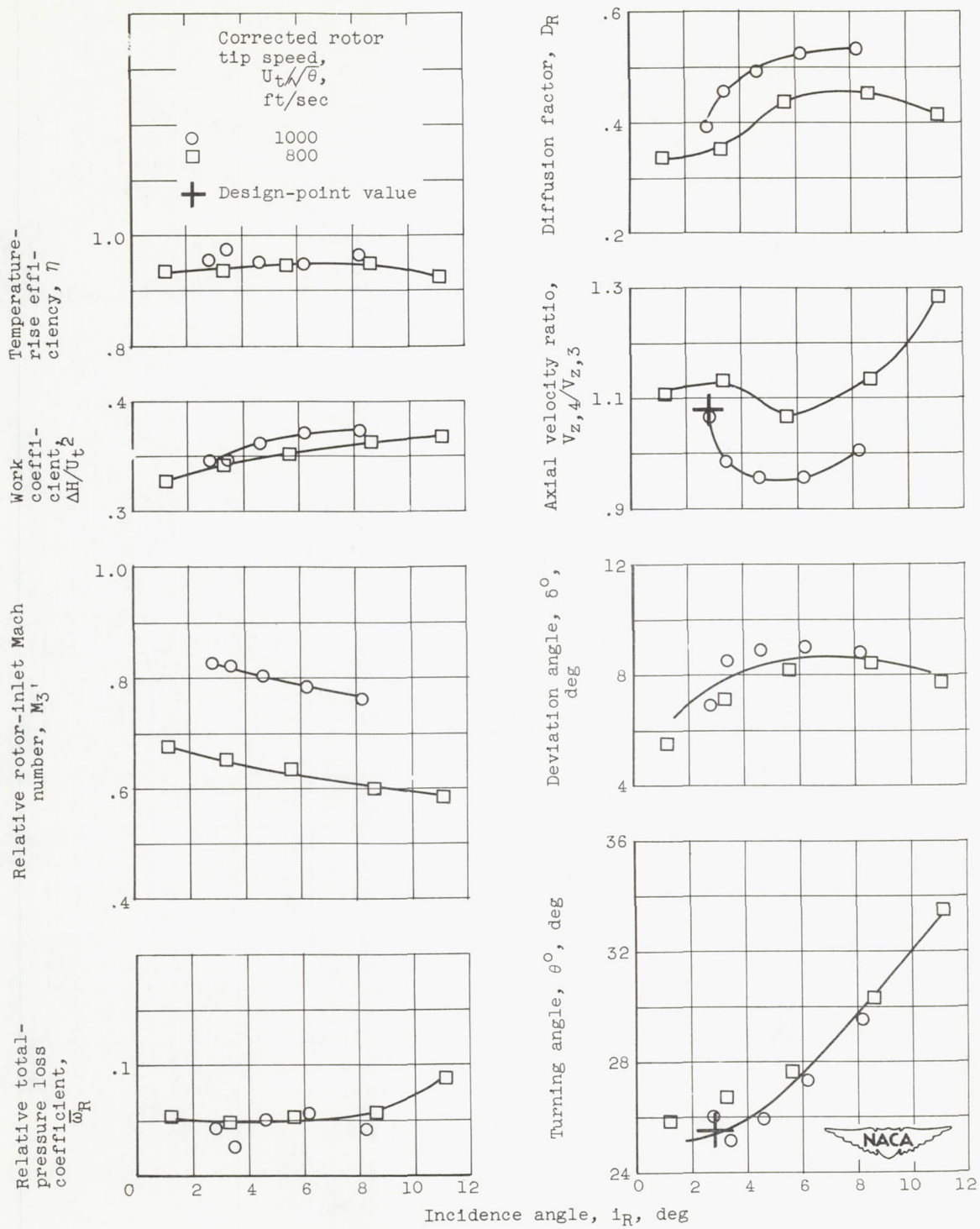

(d) Position 7; radius, 6.350 inches.

Figure 9. - Continued. Rotor-blade-element characteristics.

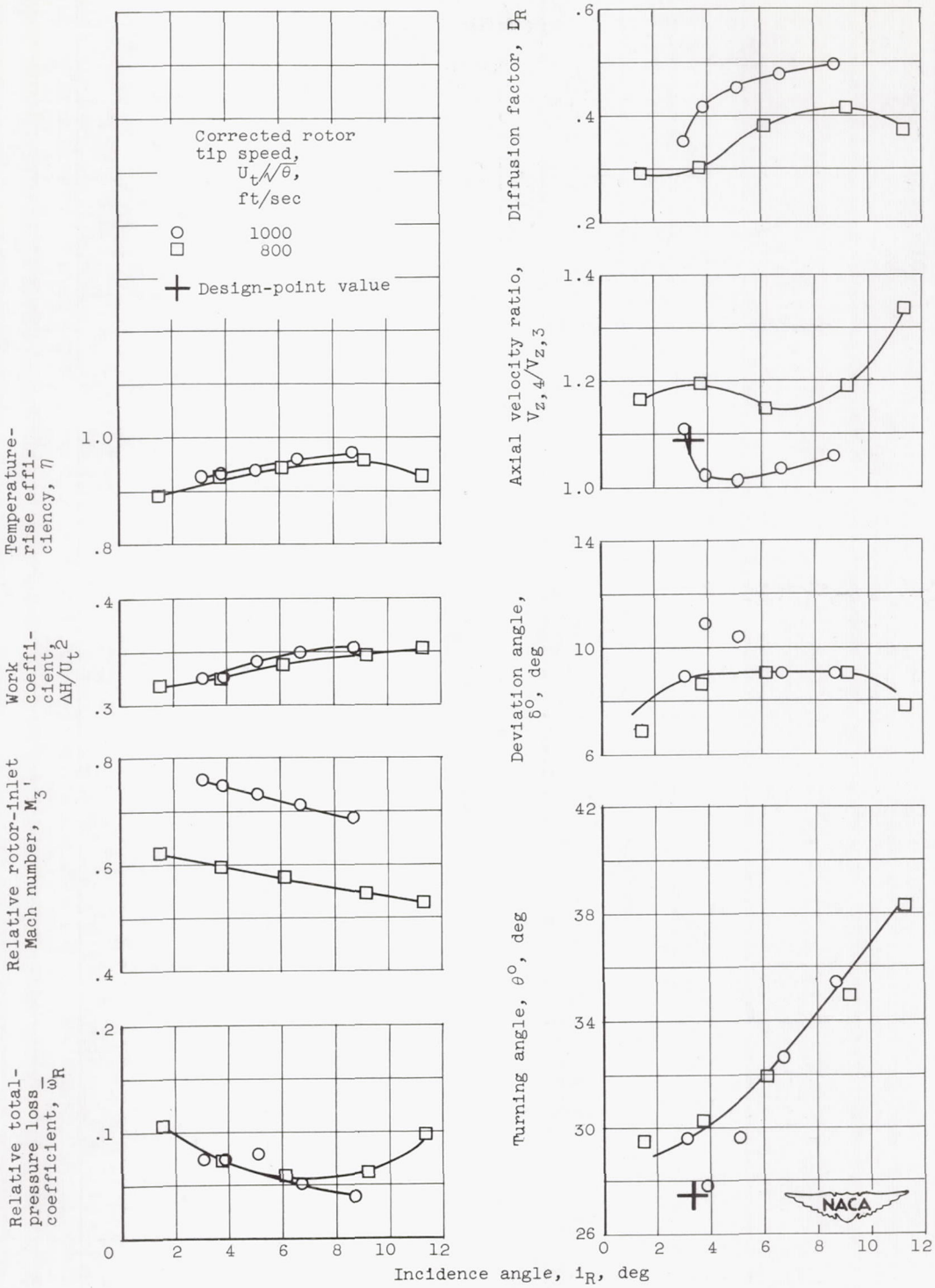

(e) Position 8; radius, 5.768 inches (near hub).

Figure 9. - Concluded. Rotor-blade-element characteristics.

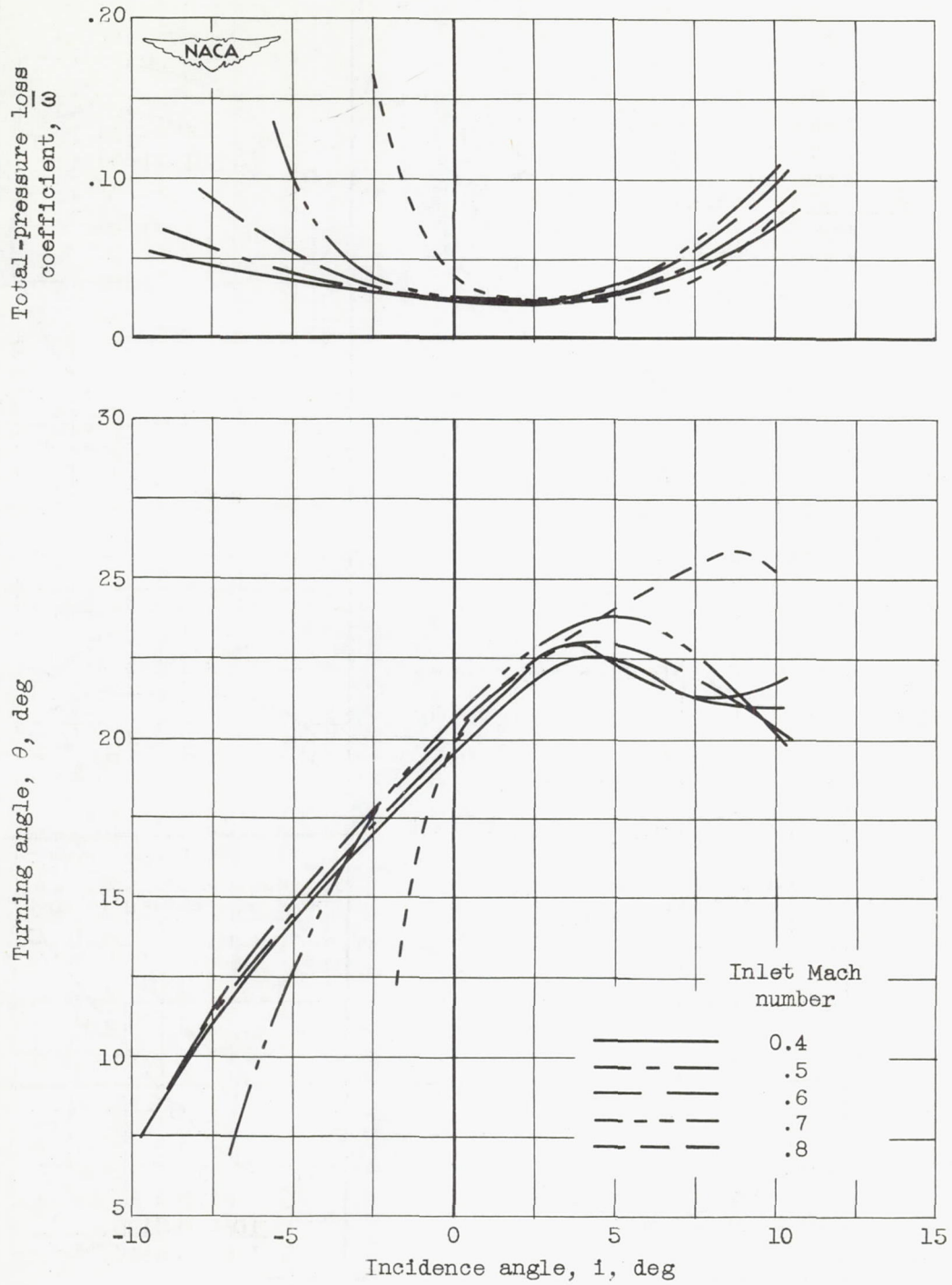

Figure 10. - Blade-element loss and turning-angle characteristics of double circular-arc profile in two-dimensional cascade reported in reference 6. Inlet air-flow angle, 55°; solidity, 1.33; camber angle, 25°; maximum thickness ratio, 10.5 percent.

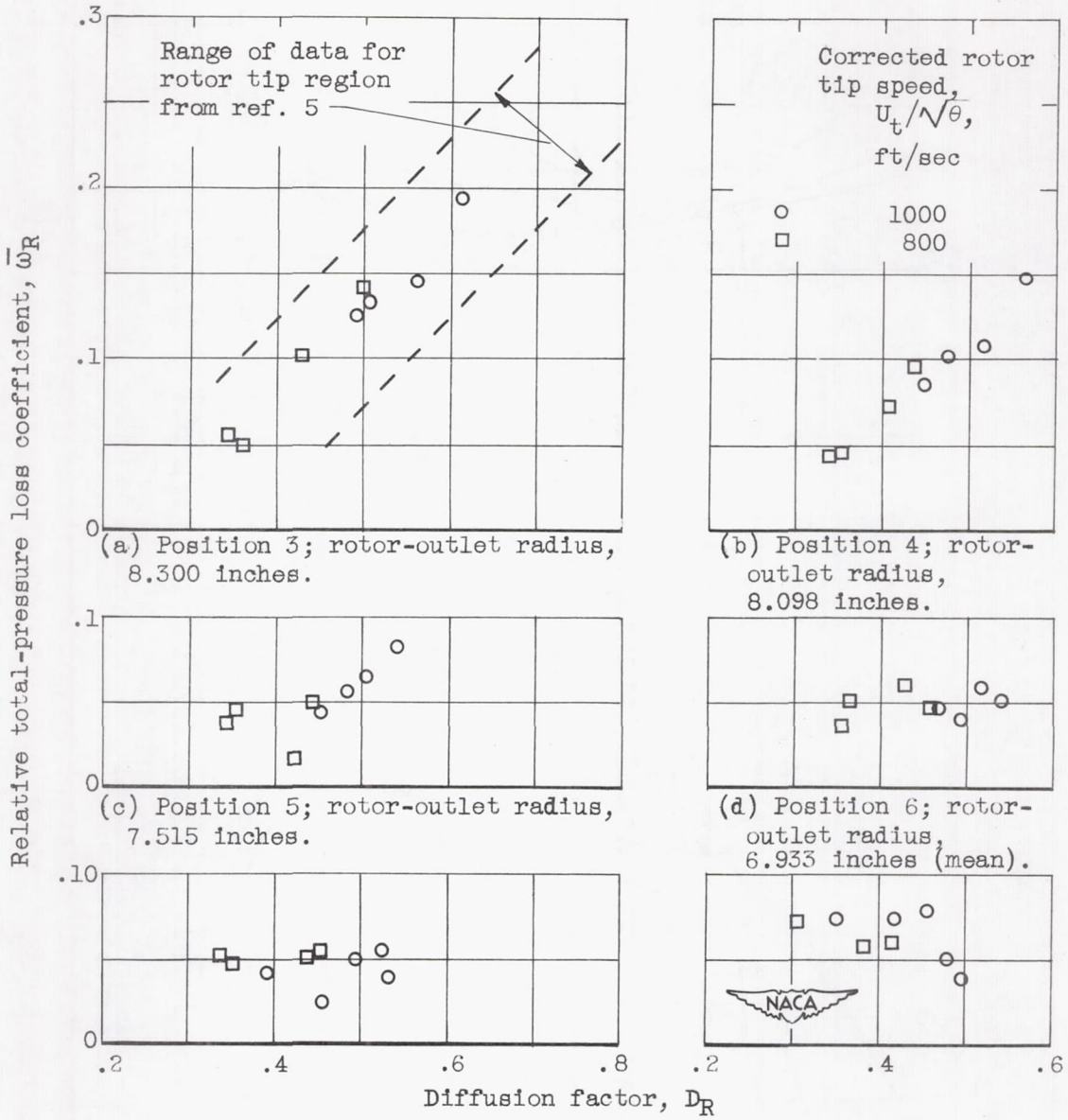

(a) Position 3; rotor-outlet radius, 8.300 inches.

(b) Position 4; rotor-outlet radius, 8.098 inches.

(c) Position 5; rotor-outlet radius, 7.515 inches.

(d) Position 6; rotor-outlet radius, 6.933 inches (mean).

(e) Position 7; rotor-outlet radius, 6.350 inches.

(f) Position 8, rotor-outlet radius, 5.768 inches.

Figure 11. - Rotor-blade-element losses against diffusion factor.

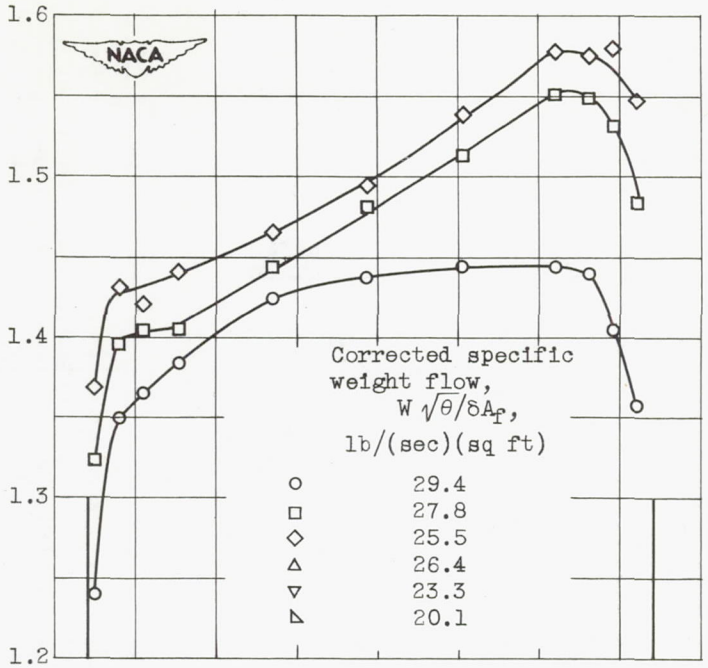

(a) Corrected rotor tip speed, 1000 feet per second.

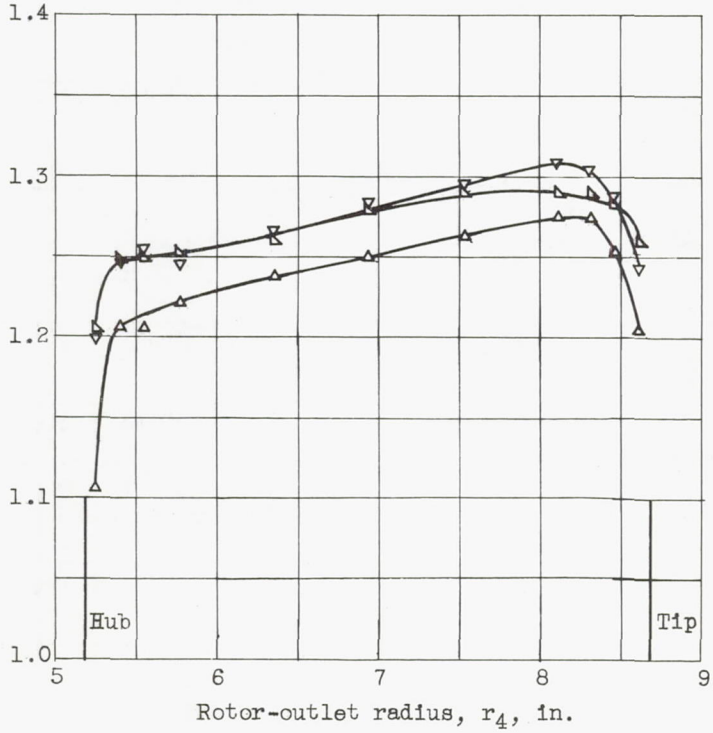

Total-pressure ratio, P_4/P_1

(b) Corrected rotor tip speed, 800 feet per second.

Figure 12. - Radial variation of rotor total-pressure ratio.

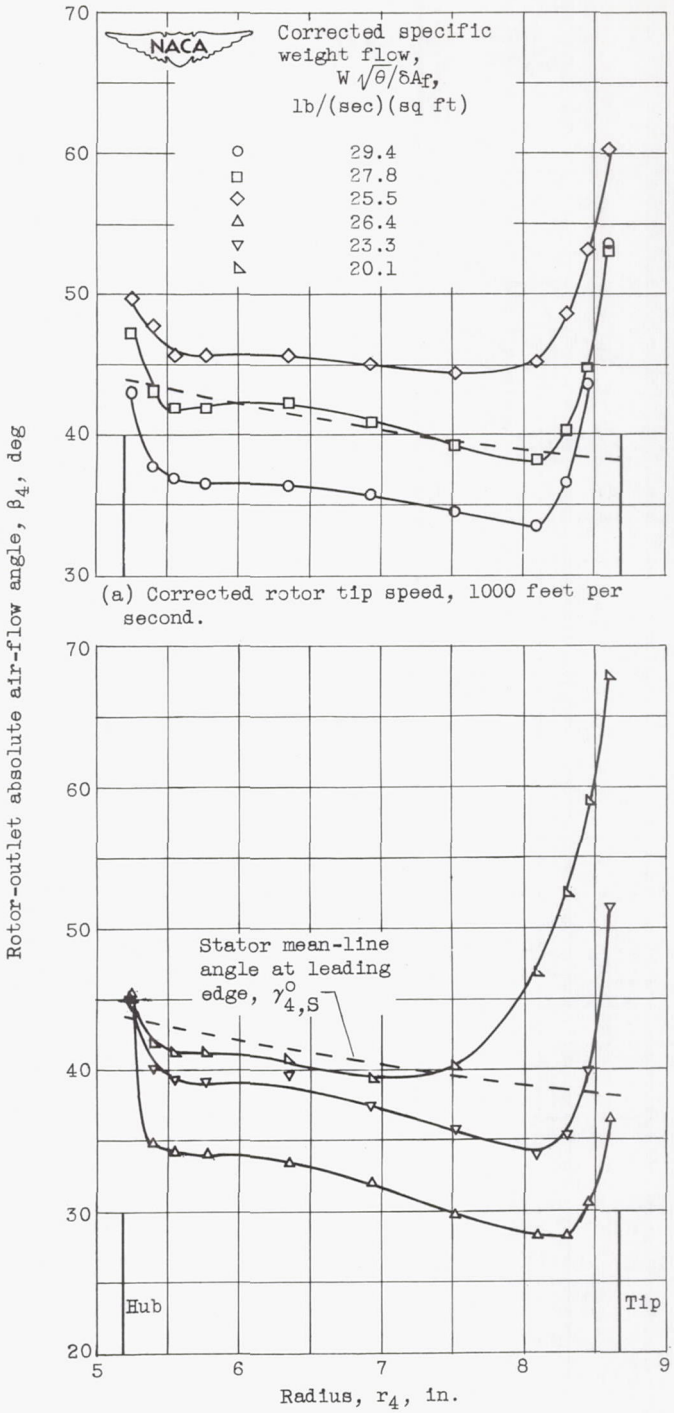

(a) Corrected rotor tip speed, 1000 feet per second.

(b) Corrected rotor tip speed, 800 feet per second.

Figure 13. - Radial variation of rotor-outlet absolute air-flow angles (station 4).

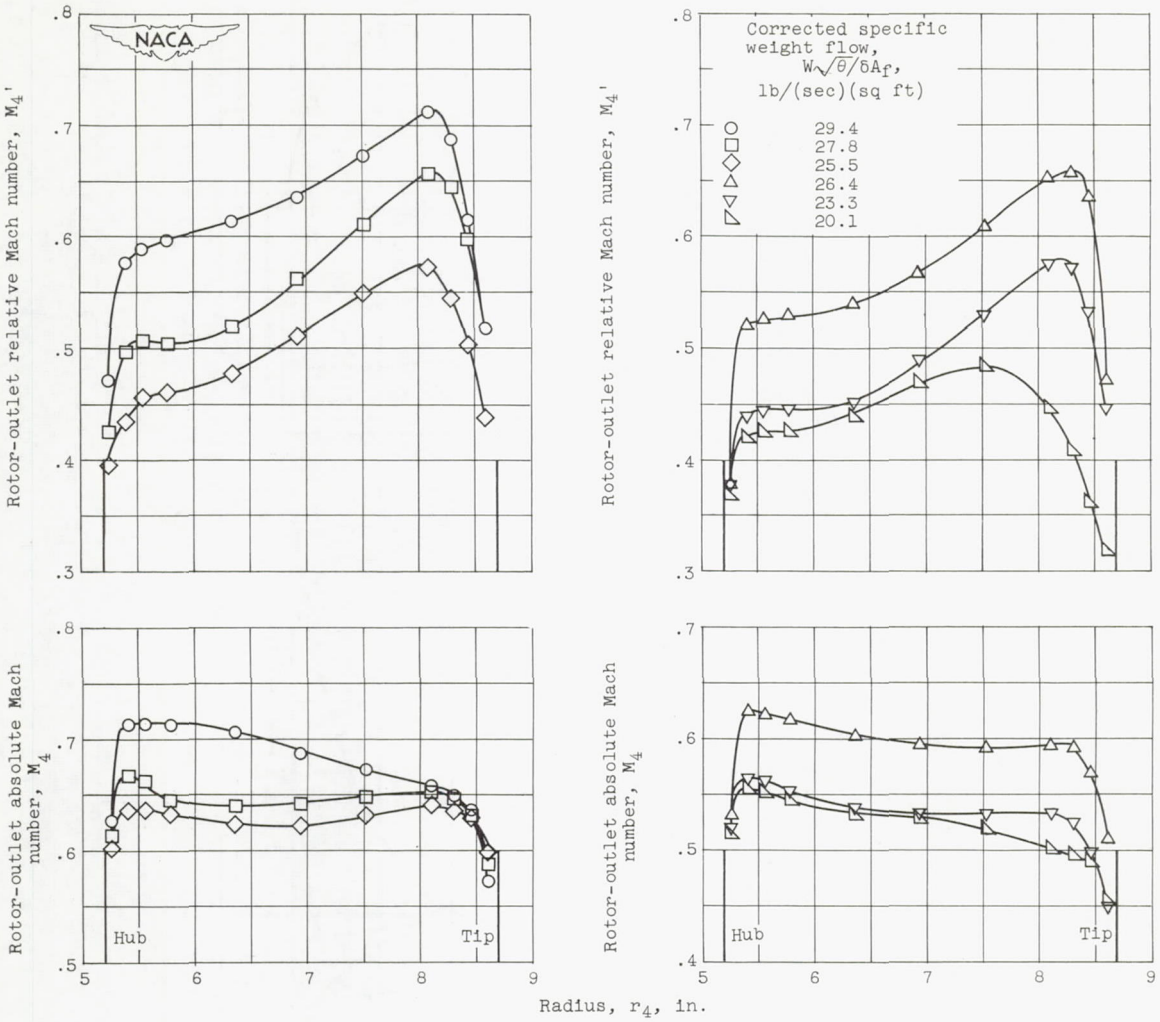

(a) Corrected rotor tip speed, 1000 feet per second.

(b) Corrected rotor tip speed, 800 feet per second.

Figure 14. - Radial variation of rotor-outlet Mach numbers (station 4).

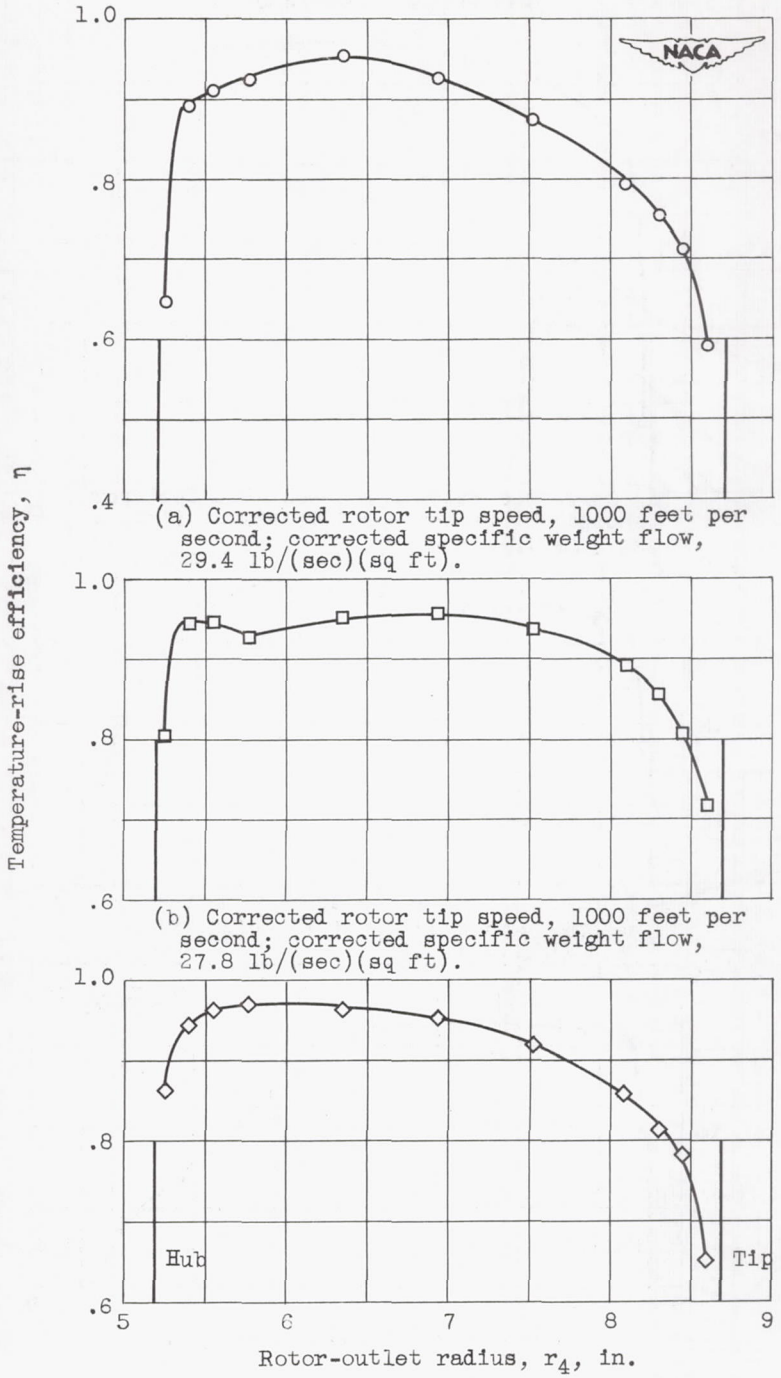

(a) Corrected rotor tip speed, 1000 feet per second; corrected specific weight flow, 29.4 lb/(sec)(sq ft).

(b) Corrected rotor tip speed, 1000 feet per second; corrected specific weight flow, 27.8 lb/(sec)(sq ft).

(c) Corrected rotor tip speed, 1000 feet per second; corrected specific weight flow, 25.5 lb/(sec)(sq ft).

Figure 15. - Radial variation of rotor-blade-element efficiency.

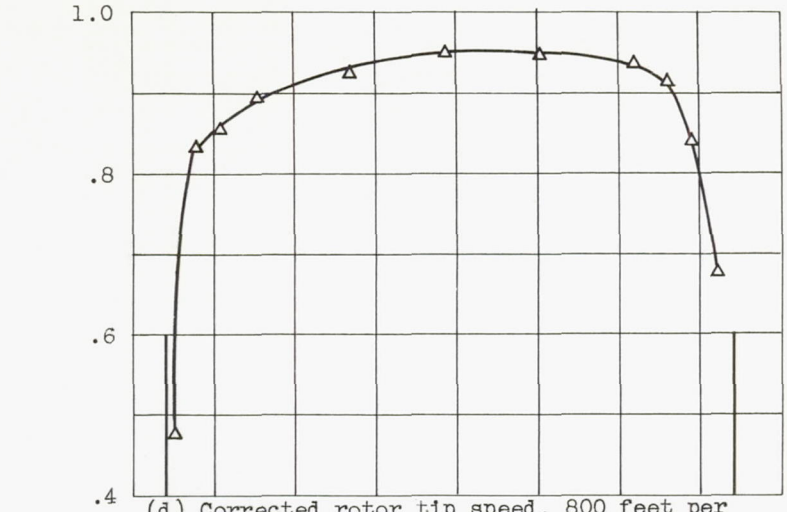

(d) Corrected rotor tip speed, 800 feet per second; corrected specific weight flow, 26.4 lb/(sec)(sq ft).

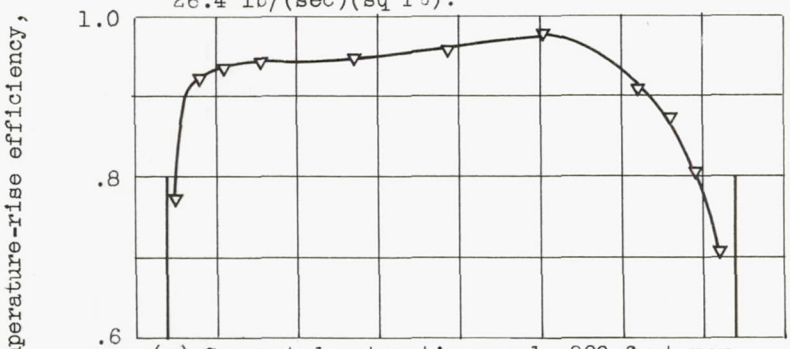

(e) Corrected rotor tip speed, 800 feet per second; corrected specific weight flow, 23.3 lb/(sec)(sq ft).

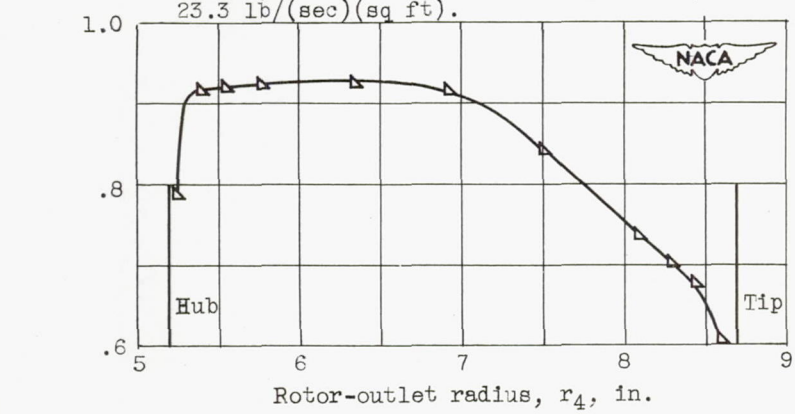

Temperature-rise efficiency, η

(f) Corrected rotor tip speed, 800 feet per second; corrected specific weight flow, 20.1 lb/(sec)(sq ft).

Figure 15. - Concluded. Radial variation of rotor-blade-element efficiency.

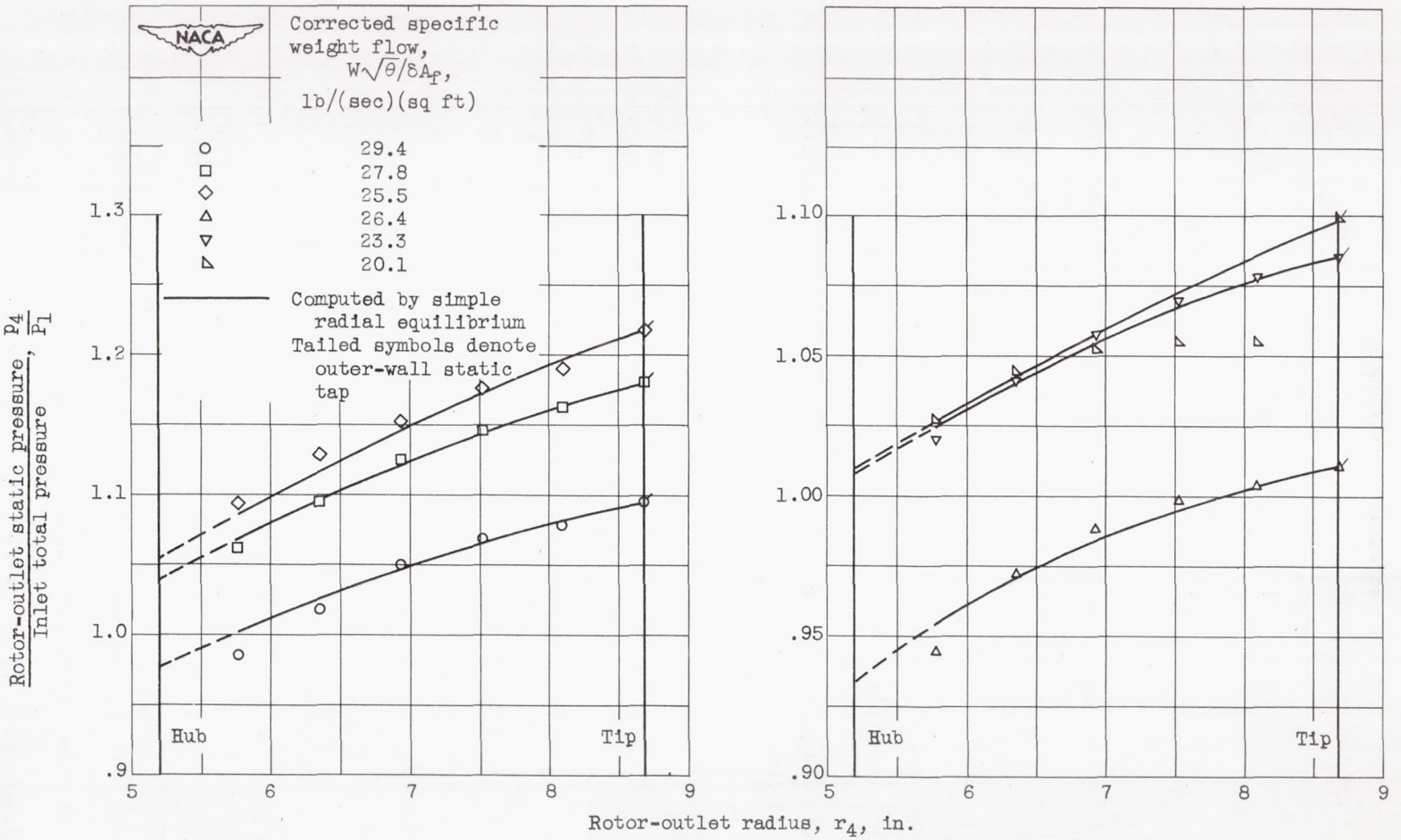

(a) Corrected rotor tip speed, 1000 feet per second.

(b) Corrected rotor tip speed, 800 feet per second.

Figure 16. - Comparison between rotor-outlet static pressures (survey) and static pressures computed by assuming simple radial equilibrium.

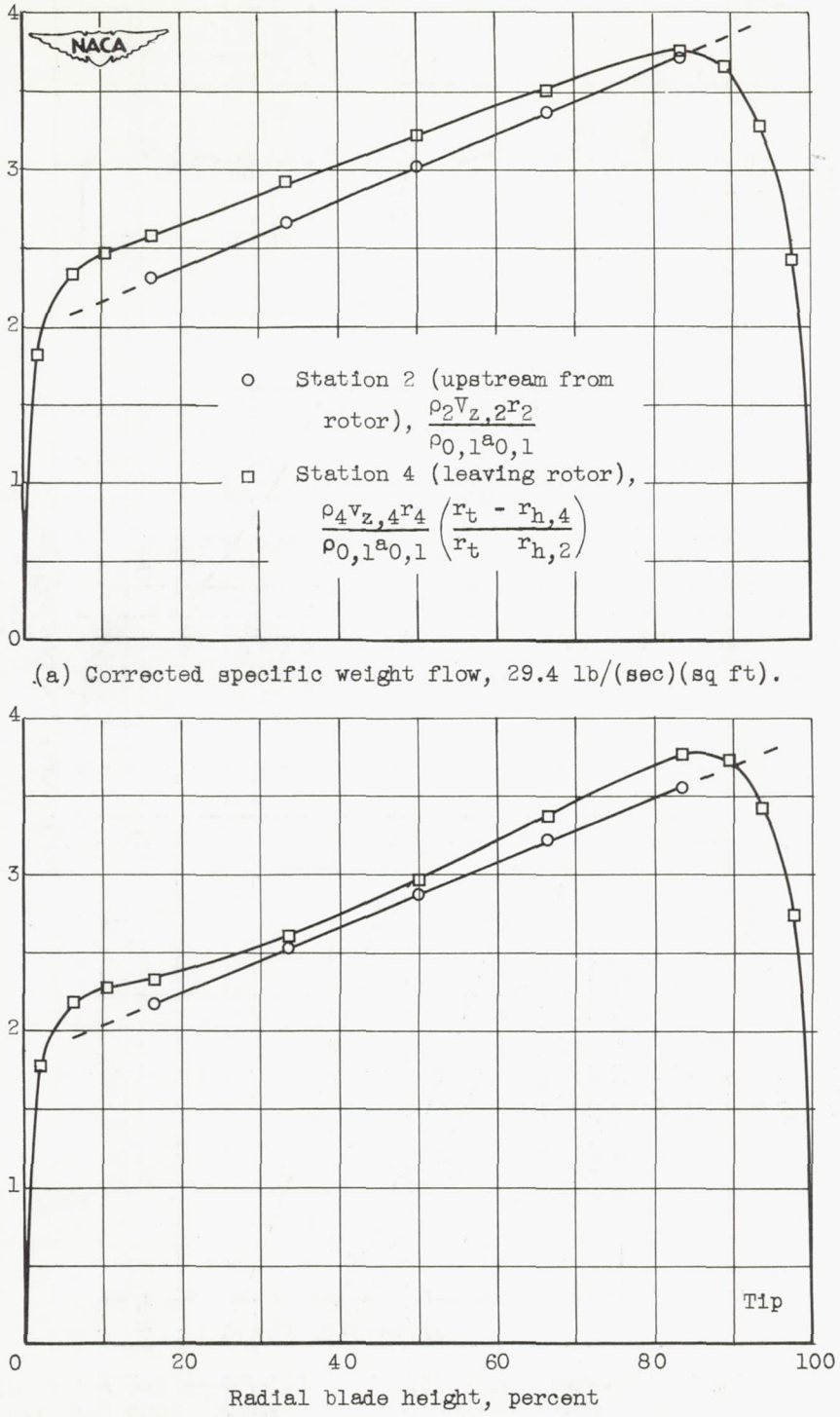

(a) Corrected specific weight flow, 29.4 lb/(sec)(sq ft).

(b) Corrected specific weight flow, 27.8 lb/(sec)(sq ft).

Figure 17. - Radial distribution of weight flow at corrected rotor tip speed of 1000 feet per second.

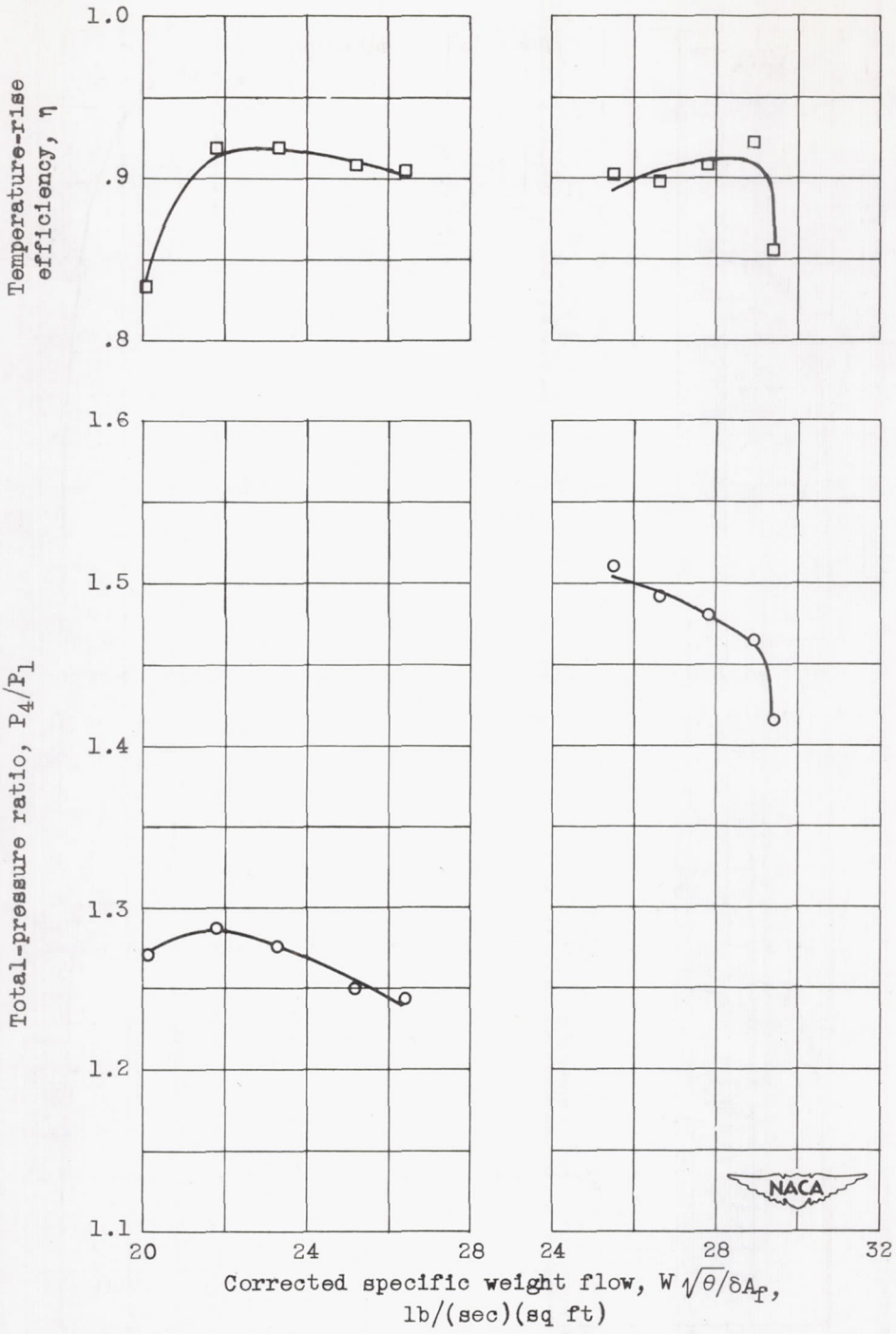

(a) Corrected rotor tip speed, 800 feet per second.

(b) Corrected rotor tip speed, 1000 feet per second.

Figure 18. - Mass-averaged rotor performance characteristics.

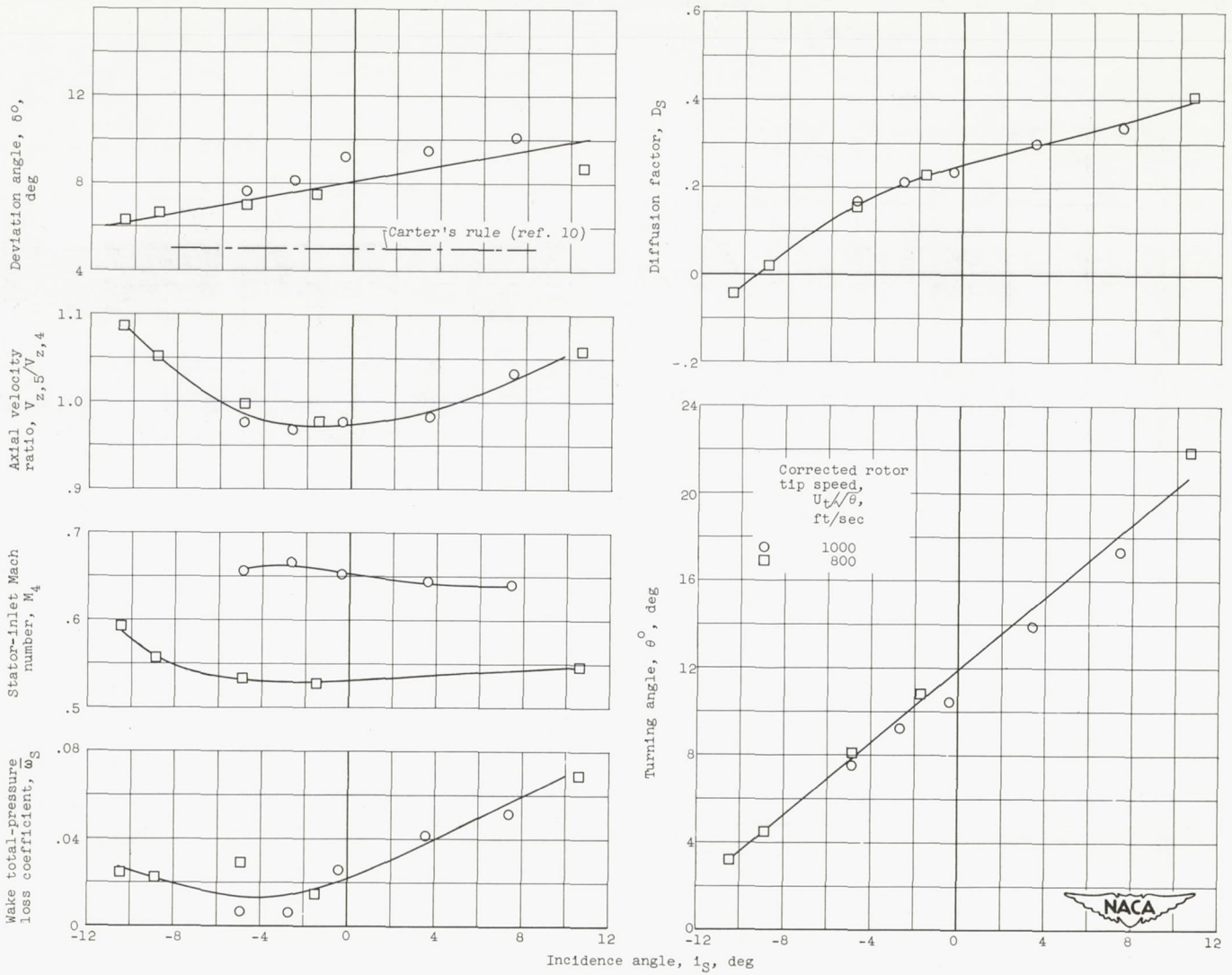

(a) Position 1; stator-outlet radius, 8.180 inches (near tip).

Figure 19. - Stator-blade-element characteristics.

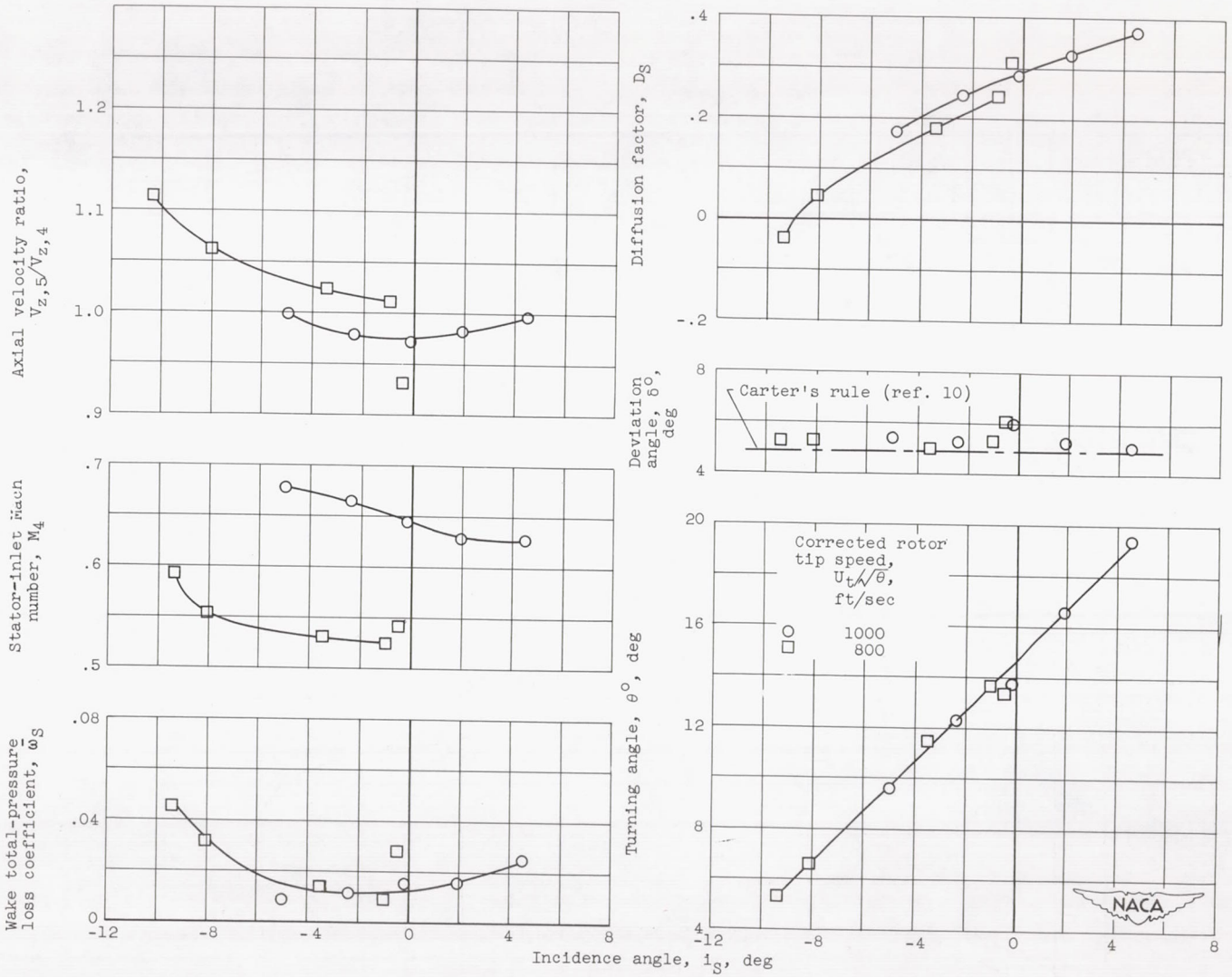

(b) Position 2; stator-outlet radius, 7.280 inches.

Figure 19. - Continued. Stator-blade-element characteristics.

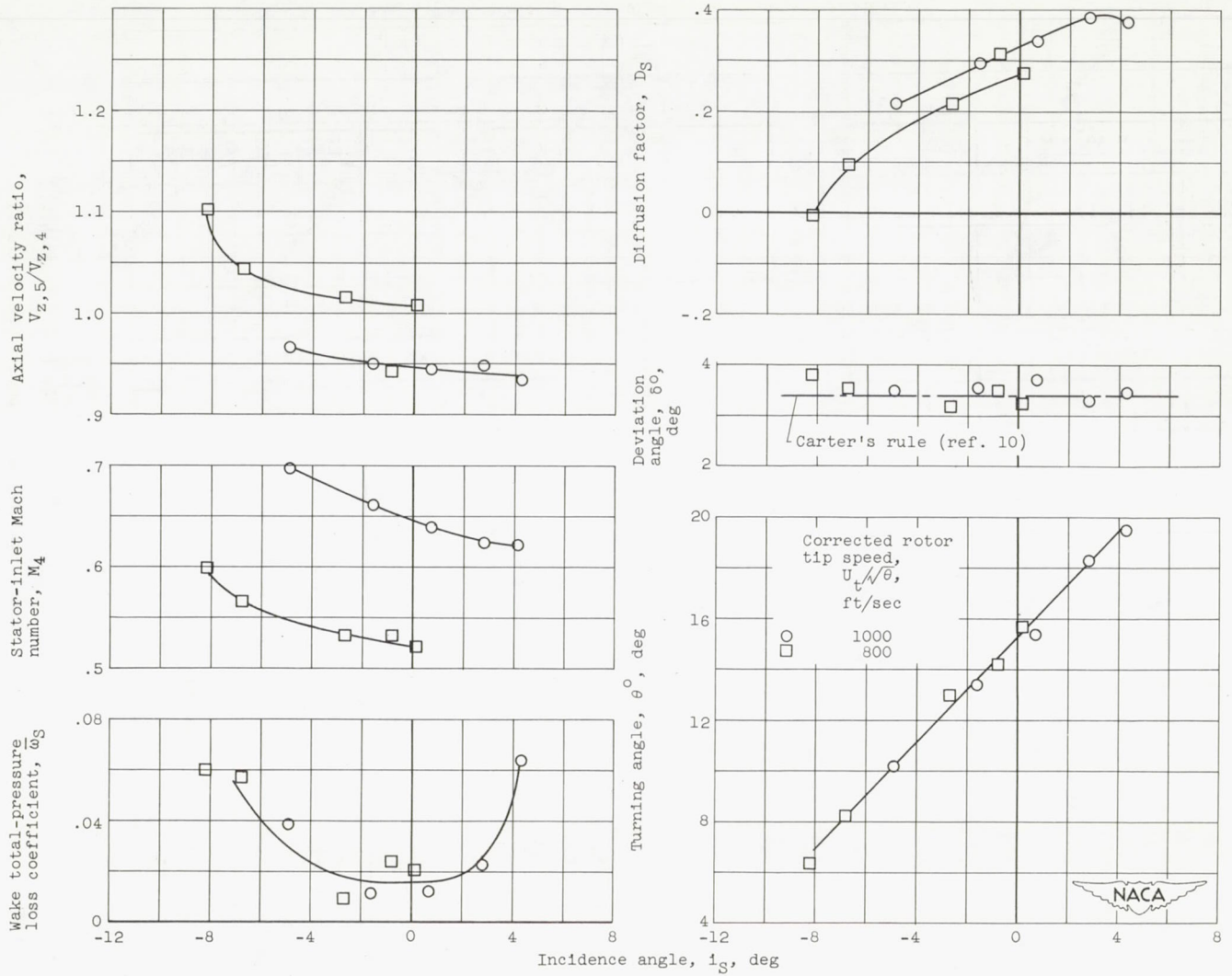

(c) Position 3; stator-outlet radius, 6.580 inches.

Figure 19. - Continued. Stator-blade-element characteristics.

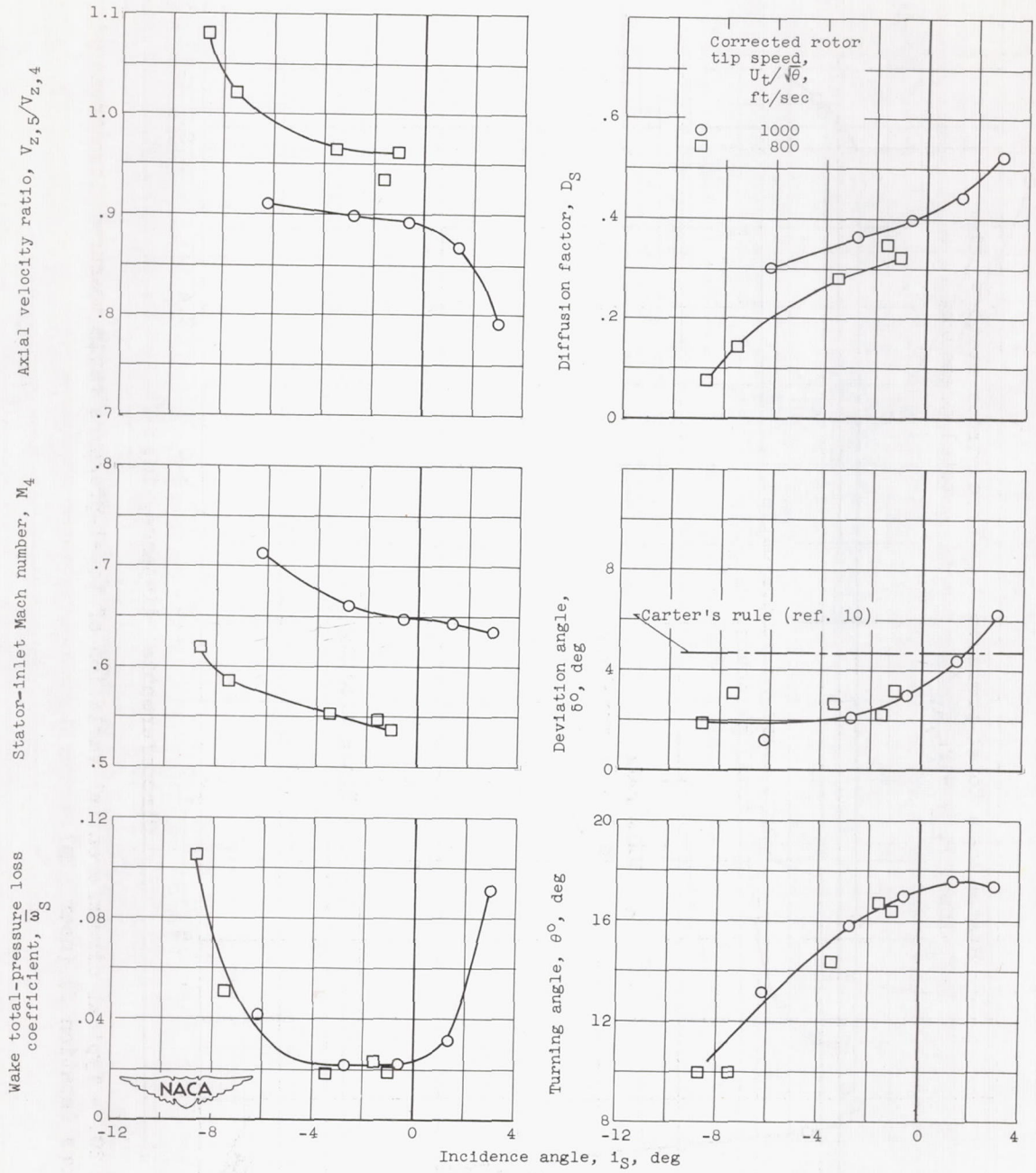

(d) Position 4; stator-outlet radius, 5.730 inches (near hub).

Figure 19. - Concluded. Stator-blade-element characteristics.

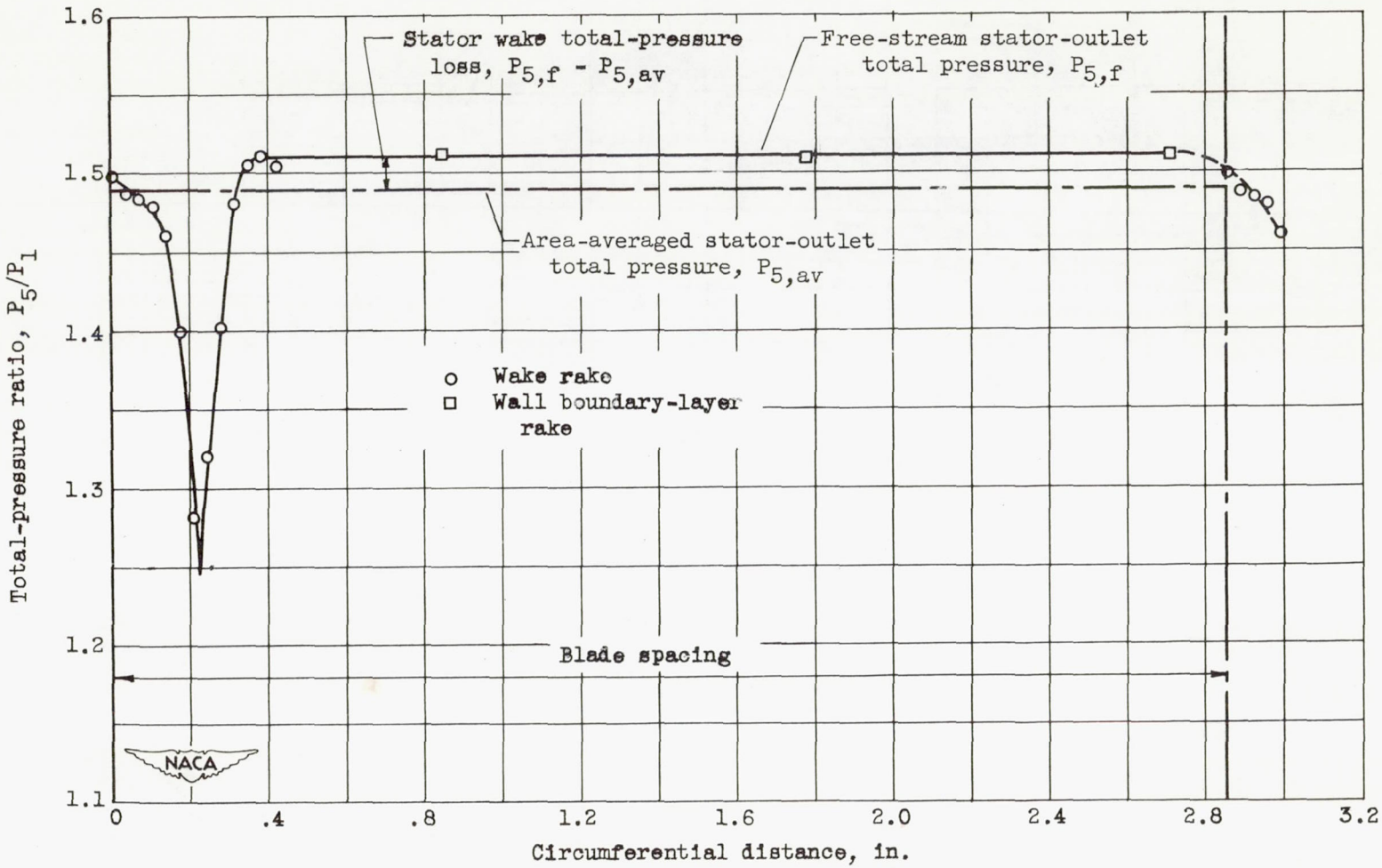

Figure 20. - Typical circumferential variation of total-pressure ratio measured downstream of stators (station 5) (near tip).

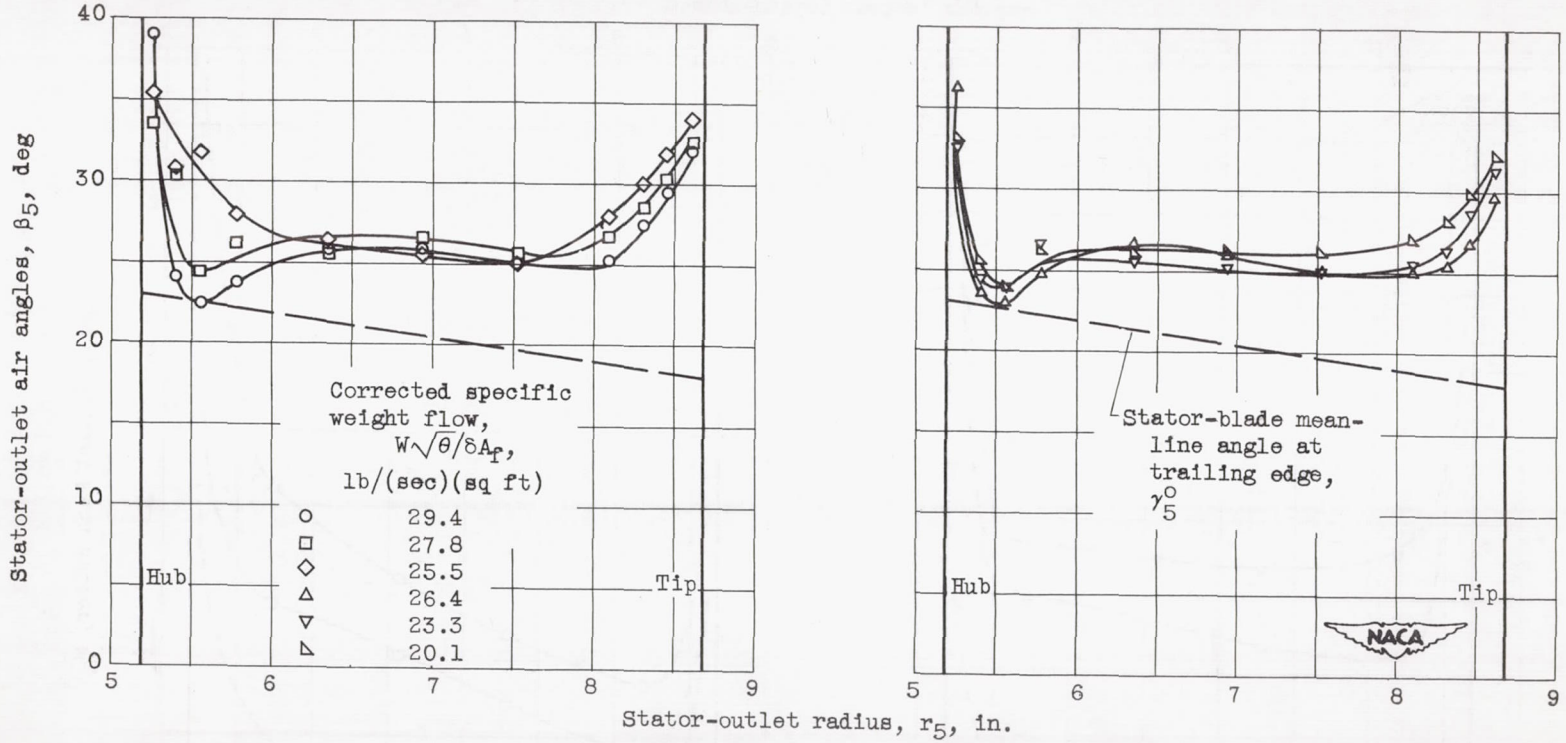

(a) Corrected rotor tip speed, 1000 feet per second.

(b) Corrected rotor tip speed, 800 feet per second.

Figure 21. - Radial variation of stator-outlet air angles (station 5).

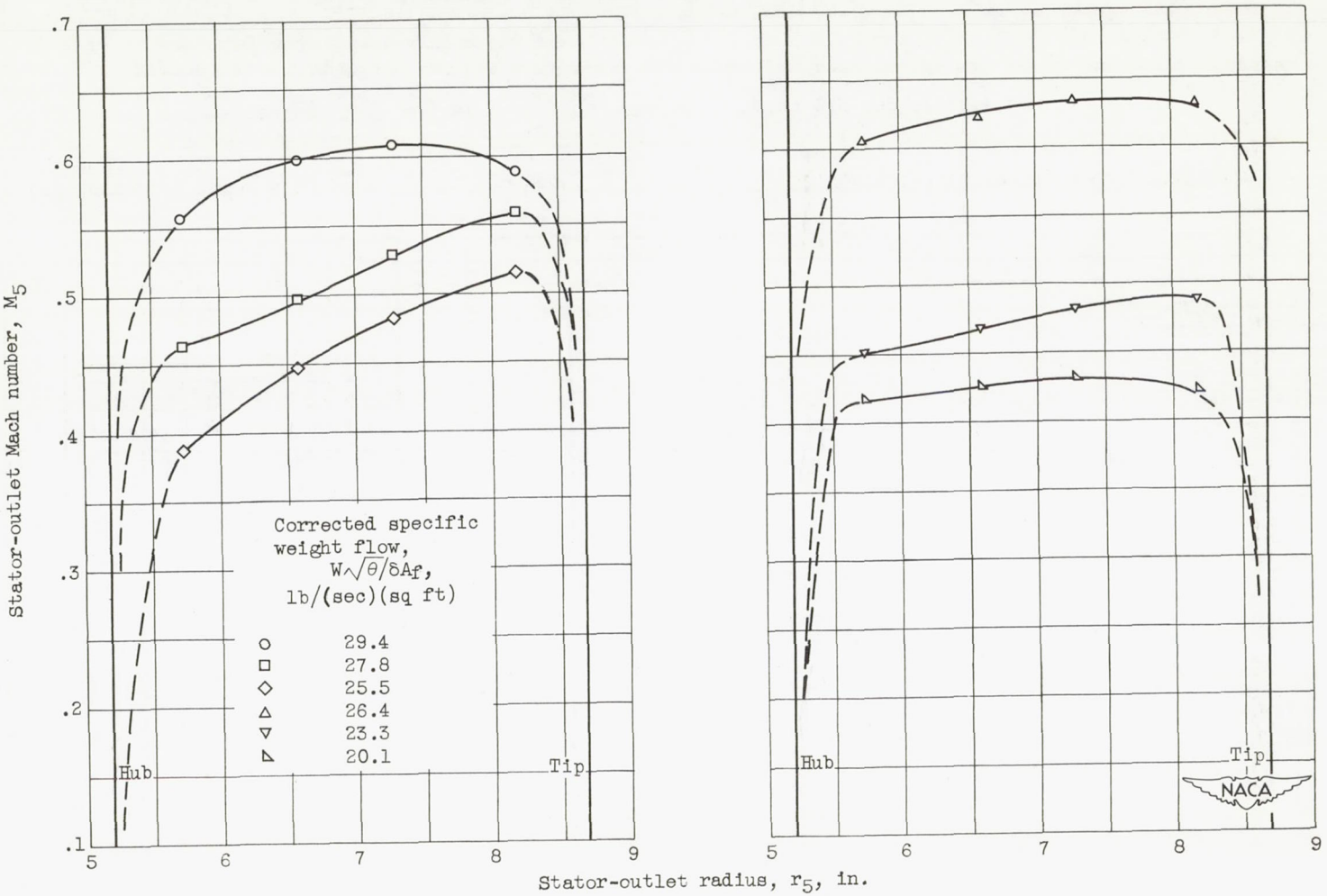

(a) Corrected rotor tip speed, 1000 feet per second.

(b) Corrected rotor tip speed, 800 feet per second.

Figure 22. - Radial variation of stator-outlet Mach number.

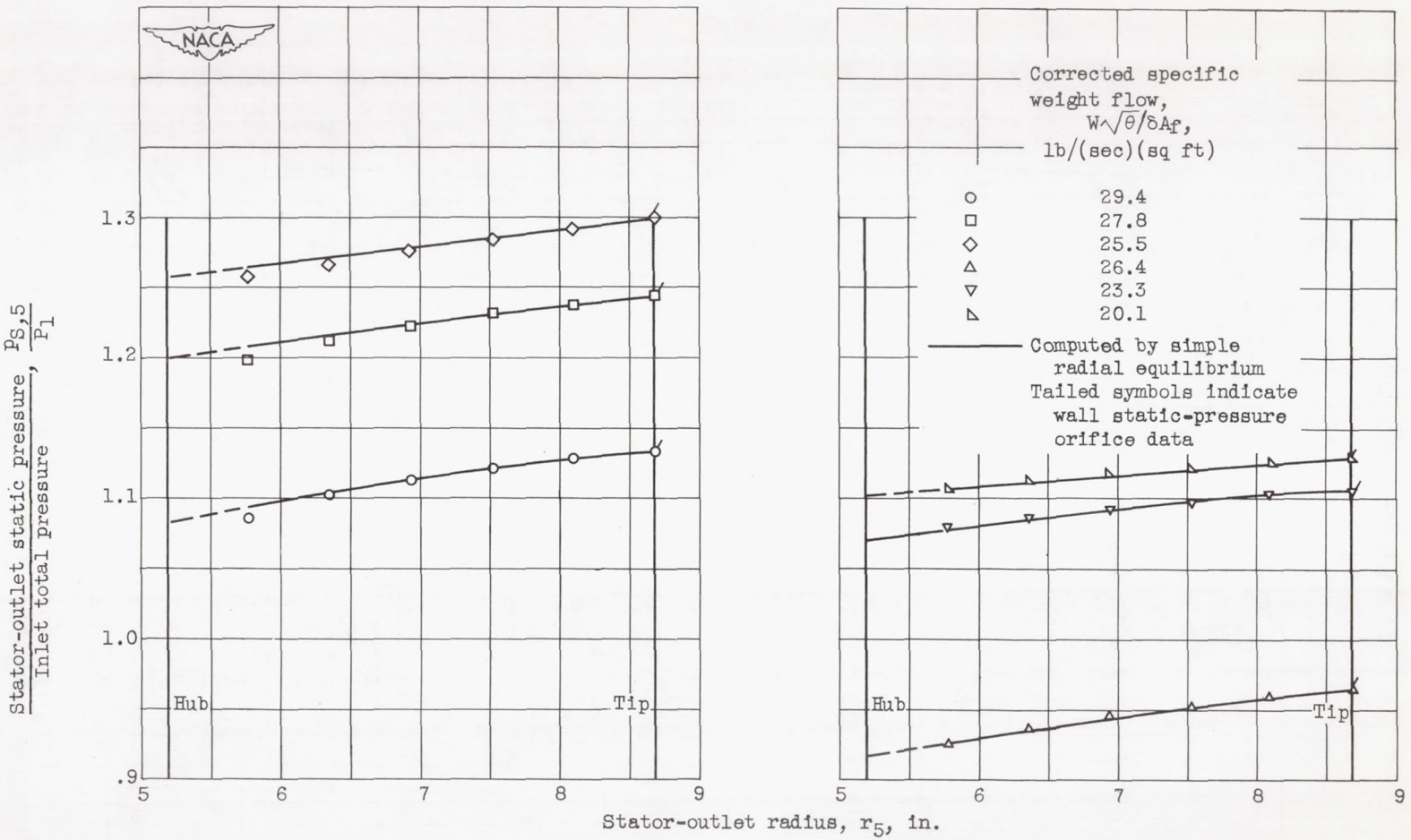

(a) Corrected rotor tip speed, 1000 feet per second.

(b) Corrected rotor tip speed, 800 feet per second.

Figure 23. - Comparison between stator-outlet survey static pressures and static pressures computed by assuming simple radial equilibrium.

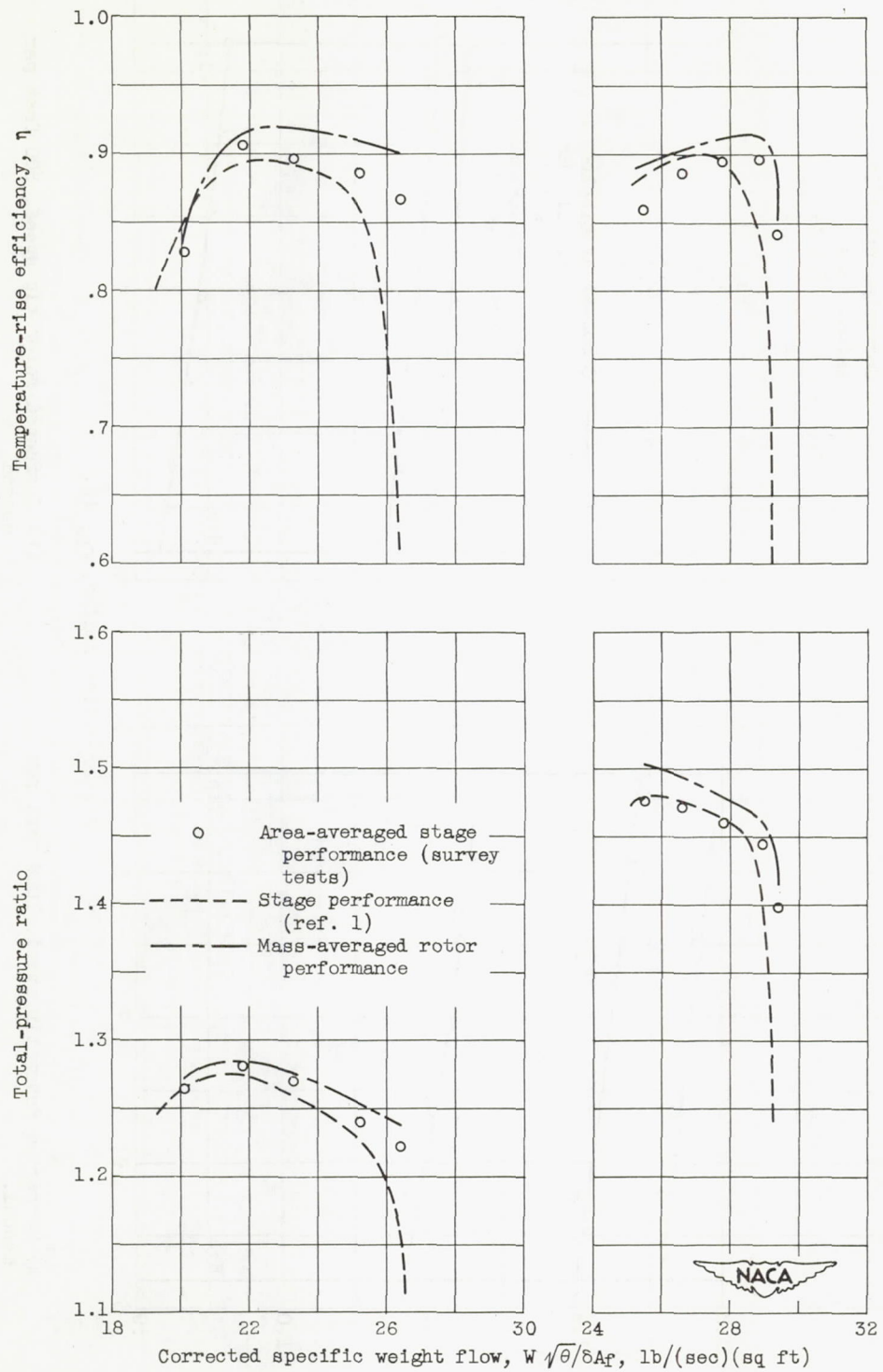

(a) Corrected rotor tip speed, 800 feet per second.

(b) Corrected rotor tip 1000 feet per second.

Figure 24. - Over-all stage performance characteristics.

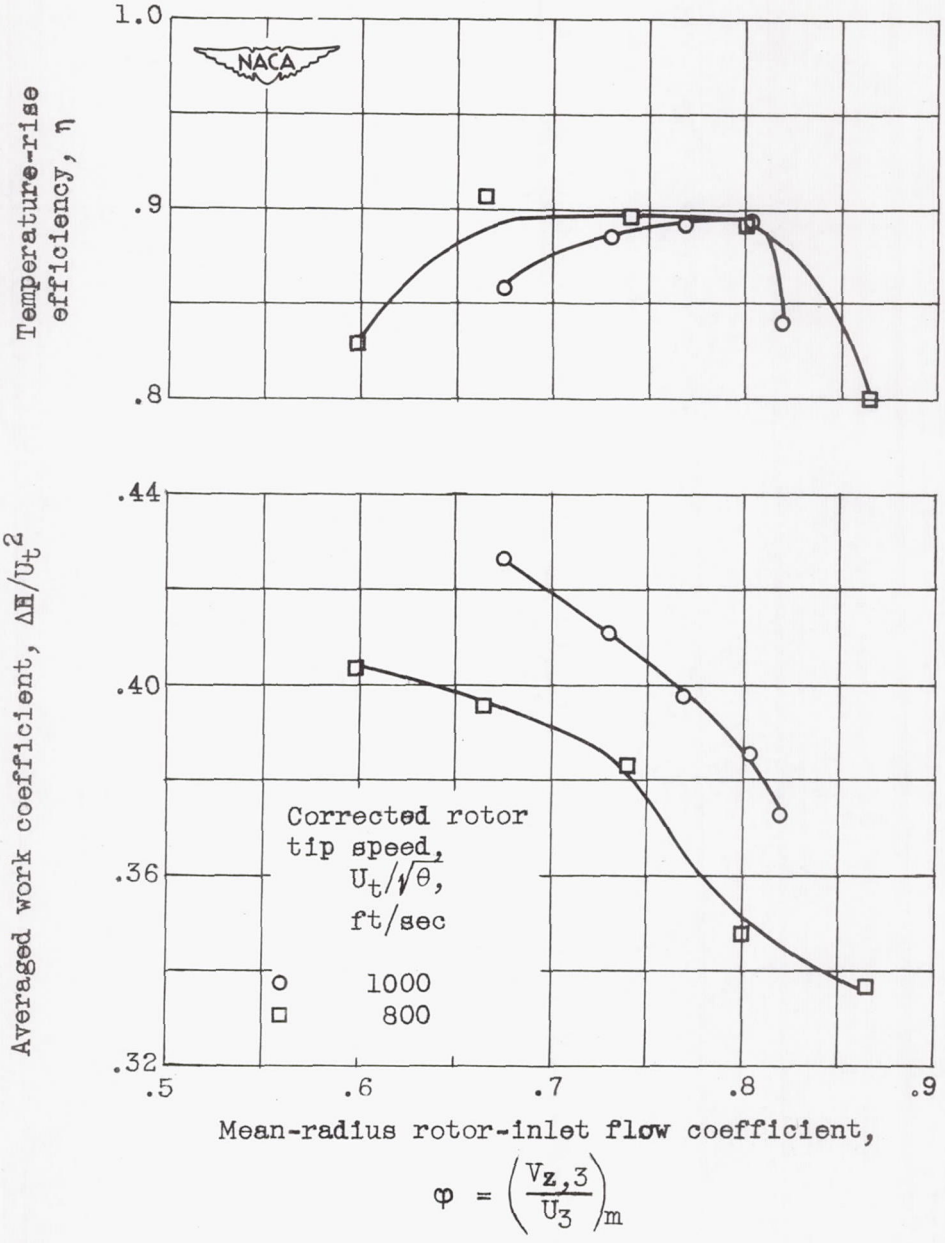

Figure 25. - Adiabatic efficiency and work coefficient for stage against flow coefficient.